Muon Isolation Efficiency Studies in the $Z^0 \rightarrow \mu\mu$ channel at the ATLAS-Detector

Diplomarbeit
zur Erlangung des akademischen Grades Diplom-Physiker

vorgelegt von

Christian Rudolph

geboren in Karl-Marx-Stadt

Institut für Kern- und Teilchenphysik
Fachrichtung Physik
Fakultät für Mathematik und Naturwissenschaften
der Technischen Universität Dresden
2009

1. Gutachter: Prof. Dr. Michael Kobel

2. Gutachter: Prof. Dr. Kai Zuber

Datum des Einreichens der Arbeit: 30.11.2009

Abstract

The investigation of the Z^0 bosons + jets production at hadron colliders can be a powerful probe to existing quantum chromodynamic calculation models as well as electroweak prediction and precision measurements. Furthermore, the $Z^0 \rightarrow \mu\mu +$ jets decay channel contributes as a major background to supersymmetric Higgs modells. Therefore, a powerful method to select $Z^0 \rightarrow \mu\mu +$ jets events is essential. This selection can be based on the usage of isolation criteria to select the final state muons.
This thesis describes a method to extract the efficiencies of different isolation criteria from measured or simulated experimental data of the ATLAS experiment at the LHC. Hereby, $Z^0 \rightarrow \mu\mu +$ jets events are selected from data first to apply isolation criteria on the final state muons and calculate the efficiency of the criteria.

Kurzfassung

Die Untersuchung der Z^0 - Boson - Produktion in Zusammenhang mit Jets an Hadronenbeschleuniger-Experimenten kann sowohl zur Überprüfung existierender Berechnungsmodelle der Quantenchromodynamik dienen als auch elektroschwache Präzisionsmessungen und Vorhersagen verifizieren. Weiterhin bildet der Zerfallskanal $Z^0 \rightarrow \mu\mu +$ Jets einen der Hauptuntergrundprozesse bei der Suche nach Higgs-Bosonen in supersymmetrischen Modellen. Aus diesen Gründen ist eine verlässliche Methode zur Selektion von $Z^0 \rightarrow \mu\mu +$ Jets - Ereignissen notwendig. Diese Selektion kann unter Verwendung von Isolationskriterien für die Zerfallsmyonen des Z^0 - Bosons erfolgen.

Die vorliegende Arbeit beschreibt eine Methode zur Bestimmung der Effizienz verschiedener Isolationskriterien aus simulierten oder gemessenen Daten des ATLAS-Experiments am LHC. In der Methode werden $Z^0 \rightarrow \mu\mu +$ Jets Ereignisse aus den Daten selektiert, um anschließend die Isolationskriterien auf die Zerfallsmyonen anzuwenden und die Effizienz der Kriterien zu bestimmen.

Contents

Chapter 1

Introduction

The development of the Standard Model (SM) in the 20th century was one of the greatest achievements for particle physics. It is capable of describing three of the four fundamental interactions of particles - the strong interaction, the weak interaction and the electromagnetic interaction - with great precision and in agreement with high energy physics experimental data.

Nevertheless, the Standard Model faces serious problems: The mechanism how fundamental particles acquire their mass is theoretically well formulated, but still lacks an experimental proof. In the most common formalism, particles acquire mass via the interaction with an omnipresent Higgs-field, whose excitations should be detectable scalar Higgs bosons. Direct and indirect searches for the Higgs-boson have failed until now, though.

Another source of uncertainties arise from the description of the strong interaction in the Standard Model. Though being mathematically precicely formulated in quantum chromodynamics (QCD), the resulting phenomenology retains large uncertainties due to the complicated mathematical structure of QCD. Phenomenologic calculations are only possible in simplified approximative models.

The Large Hadron Collider (LHC) at CERN has restarted operations in November 2009. It is a proton-proton-collider with a design center-of-mass energy of up to 14 TeV. Besides providing invaluable data to Higgs searches, it will produce all known Standard Model particles at high rates. The experimental data collected from particle collisions can thus be used to proof the Standard Model predictions and eventually to reconstruct the signature of the Higgs boson.

The ATLAS detector, one of six experiments at the LHC, is a multi-purpose particle detector sensitive to a great variety of collision event signatures. One signature of interest is the production of a Z^0 boson, accompanied by jets. In this final state, the Z^0 decaying into two muons forms a major background process to the corresponding final state arising from the Higgs decay within the minimal supersymmetric extension of the Standard Model. Furthermore, the $Z^0 \rightarrow \mu\mu$ + jets signature is a test for QCD model calculations.

This thesis investigates isolation criteria as a method to identify muons from the decay of a heavy particle such as the Z^0 boson. It determines the efficiency of different isolation criteria from simulated data on $Z^0 \rightarrow \mu\mu$ events by selecting a pure $Z^0 \rightarrow \mu\mu$ subsample and applying the isolation criteria to the muons, assuming that every muon from a Z^0 decay can be considered isolated. This experimental approach is applicable to real data without conceptual adjustments.

In the first chapter an overview is given on the theoretical framework of the Standard Model and Z^0 boson production at hadron colliders. The chapter is followed by a brief description of the experimental setup of the ATLAS detector and the LHC. Chapters four and five present common ways to reconstruct muons and $Z^0 \rightarrow \mu\mu$ events, respectively. Subsequently, the method used to determine isolation efficiencies from data is described. The results of the determination are presented in chapter seven, followed by a conclusion and outlook for further analyses.

Chapter 2

Theoretical Framework

2.1 The Standard Model of Particle Physics

The Standard Model of particle physics links quantum field theory with gauge symmetries to derive and describe the dynamics between all known fundamental particles. From experimental evidence the world consists of twelve distinctive elementary fermions (spin $\frac{1}{2}$ - particles) and their anti-particles. They can be divided into two groups:

- quarks carrying the color charge (thus interact via the strong force)
- leptons, which do not carry color charge.

Each group again consists of three generations, or families, shown in table 2.1.

Quarks			
up-type	u	c	t
down-type	d	s	b
Leptons			
neutral	ν_e	ν_μ	ν_τ
charged	e	μ	τ

Table 2.1: Quark and lepton generations.

There are four known fundamental forces:

- strong force
- weak force
- electromagnetic force
- gravitational force

The gravitational force is negligible in particle physics (that is, at the accessible energies), and cannot yet be consistently formulated in a quantum field theoretical way. It is omitted here. The forces are mediated by gauge bosons, fundamental spin-1-particles:

- strong force: eight gluons g_i

- electromagnetic force: photon γ
- weak force: two charged bosons ($W^{\pm}$), one neutral boson (Z^0)

Each of the forces can be described by applying a symmetry transformation to a Lagrange density $\mathcal{L}$ and requiring $\mathcal{L}$ to be invariant under this transformation[1]. This process introduces gauge bosons as spin-1 force carriers and coupling constants representing the strength of the force. The transformations are described by symmetry groups and named after their matrix representation.
The strong force is described by quantum chromodynamics (QCD), which requires $\mathcal{L}$ to be invariant under $SU(3)_C$-transformation. This introduces a strong coupling constant g_S (or $\alpha_s = \frac{g_S^2}{4\pi}$, respectively), a strong charge called "color" and eight color-charged massless gluons as mediating gauge bosons. The fact that gluons and quarks carry the strong charge themselves leads to the confinement of strongly-interacting particles: every quark must be in a color-singlet bound state with other quarks, free single quarks or gluons can thus not be observed [2].

The electromagnetic force is derived by requiring $\mathcal{L}$ to be invariant under the U(1)-symmetry transformation. This implies a massless chargeless photon as gauge boson.

The treatment of the weak interaction is a little more particular, as charged weak interactions have been found to be maximal parity violating, whereas neutral weak interactions are not. The charged weak bosons $W^{\pm}$ only couple to left-handed fermions and right-handed antifermions. These issues are resolved by a theory describing both electromagnetism and weak interaction in an electroweak mixing, which involves $SU(2)_L \otimes U(1)_Y$. This description implies the three-component weak isospin $\overrightarrow{I^W}$ and the weak hypercharge Y as particle properties. The electric charge Q is then given by the Gell-Mann–Nishijima relation:

$$Q = I_3^W + \frac{Y}{2} \tag{2.1}$$

The electroweak symmetry is broken to form the electromagnetic interaction with its massless gauge boson γ, and the weak interaction with three massive gauge bosons $W^{\pm}$ and Z^0. This symmetry breaking is carried out by the Higgs mechanism [3] and requires an additional scalar Higgs-boson.
An overview of all fermions and bosons and their charge properties is given in table 2.2 [4].

particles			Q	$\lvert\overrightarrow{I^W}\rvert$	I_3^W	Y	color charge	spin
$\binom{u_L}{d_L}$	$\binom{c_L}{s_L}$	$\binom{t_L}{b_L}$	$+\frac{2}{3}$	$\frac{1}{2}$	$+\frac{1}{2}$	$+\frac{1}{3}$	r,g,b	$\frac{1}{2}$
			-$\frac{1}{3}$	$\frac{1}{2}$	$-\frac{1}{2}$	$+\frac{1}{3}$	r,g,b	$\frac{1}{2}$
$\binom{\nu_{e,L}}{e_L}$	$\binom{\nu_{\mu,L}}{\mu_L}$	$\binom{\nu_{\tau,L}}{\tau_L}$	0	$\frac{1}{2}$	$+\frac{1}{2}$	-1	0	$\frac{1}{2}$
			-1	$\frac{1}{2}$	$-\frac{1}{2}$	-1	0	$\frac{1}{2}$
u_R	c_R	t_R	$+\frac{2}{3}$	0	0	$+\frac{4}{3}$	r,g,b	$\frac{1}{2}$
d_R	s_R	b_R	$-\frac{1}{3}$	0	0	$-\frac{2}{3}$	r,g,b	$\frac{1}{2}$
$\nu e, R$	$\nu_{\mu,R}$	$\nu_{\tau,R}$	0	0	0	0	0	$\frac{1}{2}$
e_R	μ_R	τ_R	-1	0	0	-2	0	$\frac{1}{2}$
		γ	0	0	0	0	0	1
		g	0	0	0	0	8 distinct	1
		W^+	$+1$	1	$+1$	0	0	1
		W^-	-1	1	-1	0	0	1
		Z^0	0	1	0	0	0	1
		H^0	0	$\frac{1}{2}$	$-\frac{1}{2}$	1	0	0

Table 2.2: Properties of fermions and gauge bosons.

2.2 The Feynman calculus and cross sections

A quantity of interest in high energy physics scattering experiments is the cross section σ of a particular process. It describes the likelihood of an interaction between particles. The aim is to calculate the total cross section of a physical process from theory and compare it with the experimental measurement. The total cross section of a particular scattering process $1 + 2 \rightarrow 3 + 4 + \ldots + n$ can be calculated using Fermi's Golden Rule:

$$\begin{aligned} \sigma &= \frac{S}{4\sqrt{(p_1 p_2)^2 - (m_1 m_2)^2}} \int \left[|\mathcal{M}|^2 (2\pi)^4 \delta^4(p_1 + p_2 - p_3 - \ldots - p_n) \right. \\ &\quad \left. \times \prod_{j=3}^{n} \left(\frac{1}{2\sqrt{p_j^2 + m_j^2}} \frac{d^3 p_j}{(2\pi)^3} \right) \right] \end{aligned} \tag{2.2}$$

Here, p_i and m_i are the momenta and masses of the involved particles i. S denotes a statistical factor that corrects for double-counting if there are identical particles in the final state. The dynamics of the process is described in its matrix element $\mathcal{M}$, while the kinematic constraints are taken care of by the phase space factor ($\prod \ldots$ and $\delta^4(\ldots)$). The calculation of the Matrix element is done in an perturbative way, and each step of the expansion can be represented by a so-called Feynman graph. An example is shown in figure 2.1.

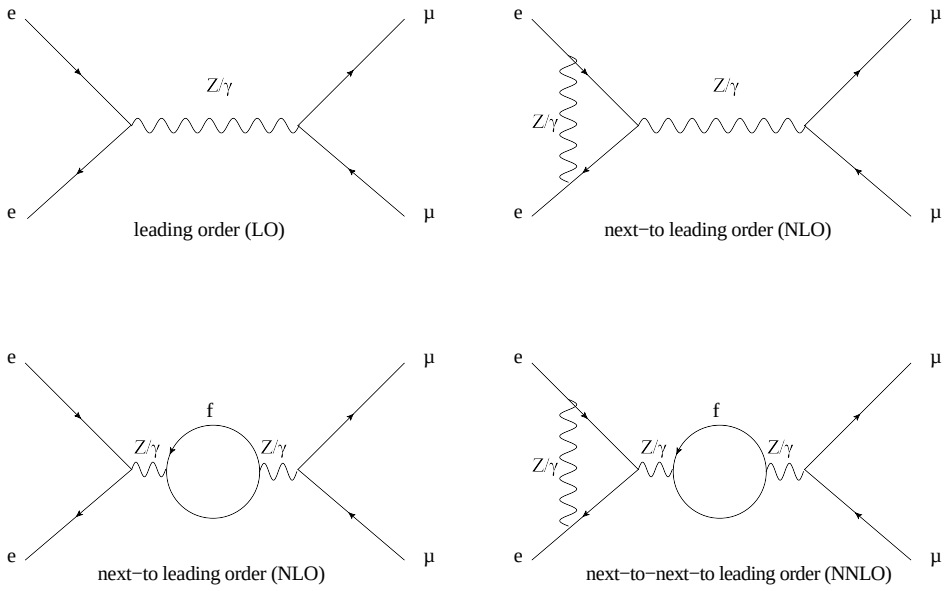

Figure 2.1: Example of Feynman graphs for the electroweak process $ee \rightarrow \mu\mu$.

The relation between cross section σ and integrated luminosity $\mathcal{L}$ can be used to calculate the expected number of detected events N_{EV} in a particular process:

$$\begin{aligned} \mathcal{L} &= \frac{N_{EV}}{\sigma \cdot \epsilon} \\ N_{EV} &= \mathcal{L} \cdot \sigma \cdot \epsilon \end{aligned} \tag{2.3}$$

given a detector efficiency ϵ which has to be determined in simulation or data.

2.3 $Z^0 \rightarrow \mu\mu$ events at hadron colliders

2.3.1 Z^0 production

The main Z^0 production channel at hadron colliders is the Drell-Yan-Process with its higher order corrections, shown in figure 2.2 The initial state particles do not occur as free particles

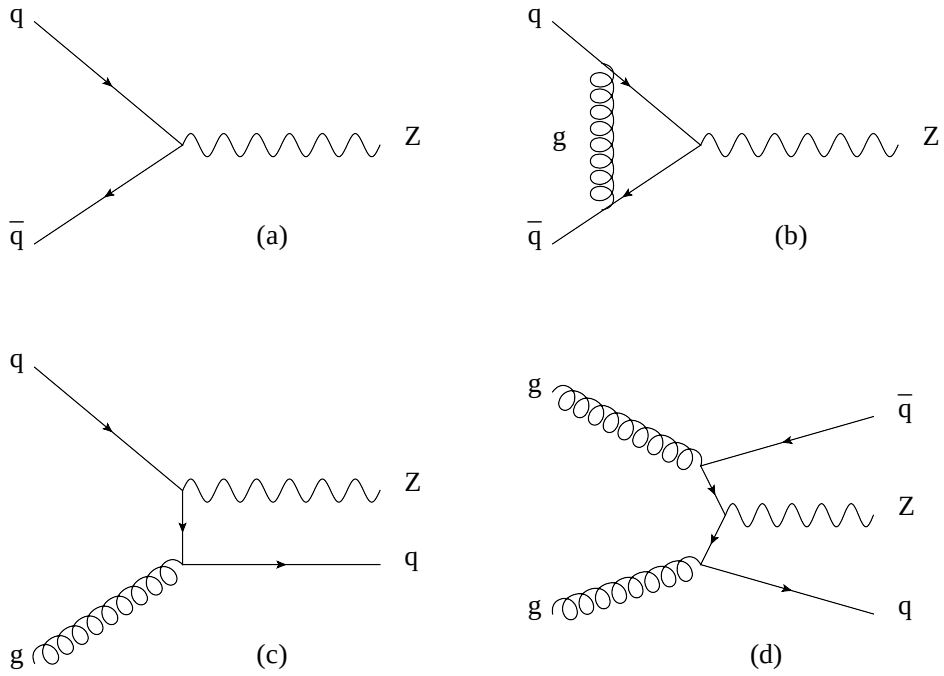

Figure 2.2: (a) Feynman graph for Z^0 production via the basic Drell-Yan process, (b) example of NLO correction, (c) NLO Drell-Yan process example with an additional quark in the final state, (d) Z^0 production via gluon fusion with an additional quark-antiquark-pair in the final state

due to the confinement of the strong interaction(see section 2.1, [1]), but are trapped in protons (or antiprotons, respectively) of the accelerator beam. In calculations of the inclusive Z production cross section, models describing the parton distribution function (PDF) are used as kinematic input. The total cross section can thus be calculated in perturbative QCD via the following ansatz:

$$\begin{aligned}\sigma_{tot}(pp' \rightarrow (Z \rightarrow l_1 l_2)X) &= \sum_{a,b=q,\bar{q},g} \int dx_1 dx_2 f_{a/p}(x_1,\mu_F) f_{b/p'}(x_2,\mu_F) \\ &\quad \times \widehat{\sigma}_{tot}(a+b \rightarrow Z^0 + X \rightarrow l_1 l_2 + X). \end{aligned} \tag{2.4}$$

l_1, l_2 are the charged lepton and antilepton from the Z^0 decay, $\widehat{\sigma}_{tot}$ denotes the hard scattering cross section and $f_{a/p}(x_1,\mu_F), f_{b/p'}(x_2,\mu_F)$ equal the parton distribution functions. Equation 2.4 has to be integrated over the parton momentum fractions inside the proton x_1, x_2 and summed over all relevant parton flavors a, b. μ_F is the strong factorisation scale[5]. Higher order corrections to 2.4 f_i or $\widehat{\sigma}_{tot}$ originate from irradiation of additional real or virtual particles within the strong or electroweak interaction. Due to the respective coupling constants, the

strong corrections contribute by a factor 100 more than additional weak contributions[6]. The QCD corrections have been evaluated until next-to-next-to-leading order, whereas electroweak corrections have been calculated until next-to-leading order.

2.3.2 Theoretical Uncertainties

Theoretical uncertainties for predictions of inclusive cross sections for $Z^0 \rightarrow \mu\mu$ events at hadron colliders arise from parton distribution functions[7] exhibiting large uncertainties in phase space regions accessible here. The choice of the factorisation scale and renormalization scale introduce another source of theoretic uncertainty. To allow perturbative calculations, QCD has to be renormalized[8]. Thus the strong coupling constant α_S is replaced by a running coupling, depending on the chosen renormalization scale μ and the transferred momentum Q^2 in the interaction process [9]:

$$\alpha_S(Q^2) = \frac{\alpha_S(\mu^2)}{1 + \frac{\alpha_S(\mu^2)}{12\pi}(33 - 2n_f)\ln(Q^2/\mu^2)} \tag{2.5}$$

In equation 2.5, n_f equals the number of quark flavours, depending on the considered energy range. In case of low transferred momenta ($Q^2 \ll \mu^2$), α_S diverges as do other QCD observables, and perturbation theory cannot be used to calculate cross sections. The factorization scale μ_F[5] separates the perturbative and non-perturbative parts in the calculation: The parton distribution functions $f_{a/p}(x_1, \mu_F), f_{b/p'}(x_2, \mu_F)$ in equation 2.4 are not computable in perturbative QCD and thus must be measured in experiments and extrapolated to the chosen factorization scale. The hard scattering cross sections $\widehat{\sigma}_{tot}$ in equation 2.4 can then be calculated in perturbative QCD, depending on the same factorization scale.
Explicit order-by-order cross section calculation using equation 2.4 and the perturbative computable hard scattering cross section $\widehat{\sigma}_{tot}$ is difficult. The more final state particles occur (in this case the number of additional final state partons), the more orders of α_S are involved in the calculation and uncertainties increase. In Monte-Carlo event generators, only the leading or next-to-leading order are thus calculated explicitely, and additional final state partons are generated via the parton shower approach.

The partons are assigned a transition probability to irradiate another parton, e.g. $q \rightarrow qg$, which is calculated using the so-called leading logarithm approximation in perturbative QCD[2]. This approximation is suitable for low transferred momenta during the parton irradiation which complements the matrix element calculation suitable for a high transferred momentum. Thus if parton shower algorithms are used to achieve better predictability in addition to the hard (tree-level) matrix element calculation, their outputs have to be matched to avoid double-counting of parton emissions.

Since these approximations are used during the total cross section calculation for the process $pp' \rightarrow (Z^0 + X) \rightarrow (\mu\mu + X)$, the measurement of this cross section is a test for the validity of these approximations. A Z^0 + Jets cross section measurement can thus probe the choice of the renormalization scale, the factorization scale, the leading and next-to-leading order matrix element calculation and the parton shower matching, improving the mathematical description of QCD.

Results of the cross section calculation are presented in figure 2.3. The discrepancy between measured data and theoretical prediction is clearly visible.

The values of the total cross section $\sigma_{pp' \rightarrow (Z^0+X) \rightarrow (\mu\mu+X)}$ are summarized in table 2.3[10].

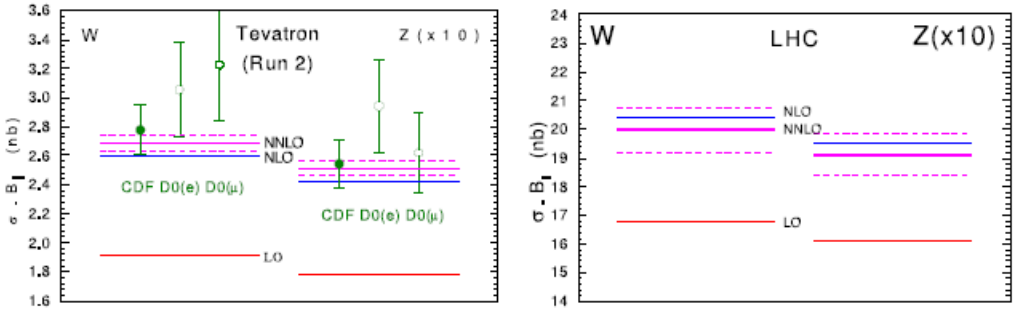

Figure 2.3: Inclusive cross sections[7] for W and Z production at the Tevatron ($\sqrt{s} = 1.96TeV$) and LHC ($\sqrt{s} = 14TeV$), compared with Tevatron measurements.

Tevatron, ($\sqrt{s} = 1.96$TeV)	$\sigma_Z \cdot B_{ll}$ (nb)
LO	$0.1788^{+0.0023}_{-0.0025}$
NLO	$0.2426^{+0.0054}_{-0.0043}$
NNLO	$0.2507^{+0.0048}_{-0.0041}$
LHC, ($\sqrt{s} = 10$TeV)	$\sigma_Z \cdot B_{ll}$ (nb)
LO	$1.163^{+0.011}_{-0.017}$
NLO	$1.309^{+0.029}_{-0.027}$
NNLO	$1.429^{+0.024}_{-0.022}$
LHC, ($\sqrt{s} = 14$TeV)	$\sigma_Z \cdot B_{ll}$ (nb)
LO	$1.736^{+0.019}_{-0.028}$
NLO	$2.001^{+0.040}_{-0.032}$
NNLO	$2.051^{+0.035}_{-0.033}$

Table 2.3: Predicted theoretical Z^0 cross sections[10] at the Tevatron($\sqrt{s} = 1.96$TeV) and the LHC($\sqrt{s} = 10\text{TeV}, 14\text{TeV}$). The cross sections are multiplied with the branching ratio B_{ll} for the Z^0 decaying into two leptons (e^+e^- or $\mu^+\mu^-$. Cross sections are given for leading order (LO), next-to-leading order (NLO) and next-to-next-to-leading order (NNLO).

2.3.3 Muon interaction with detector material

In this chapter the interaction of muons with the detector material will be investigated. Muons are charged leptons of intermediate mass (see table 2.4), so they interact via the electromagnetic and weak forces, but not via the strong force. Although the muon is not

lepton flavor	mass (MeV)	mean lifetime	main decay channel(s)
e	0.511	stable	–
μ	105.66	2.197	$e^-\overline{\nu_e}\nu_\mu$
τ	1776.84	$290.6 \times 10^{-15} s$	$\mu^-\overline{\nu_\mu}\nu_\tau$
			$e^-\overline{\nu_e}\nu_\tau$
			$\pi^-\nu_\tau$
			$\pi^-\pi^0\pi^0\nu_\tau$
			$\pi^-\pi^+\pi^-\nu_\tau$

Table 2.4: Properties of the charged leptons[4]. The main decay channel(s) are only given for the negatively charged lepton, for the antileptons the decays are similar but charge-conjugated.

stable, it can travel a long distance before its decay, provided a high momentum. If a muon traverses matter, it looses energy due to electromagnetic interaction. In principle this includes two different processes:

- bremsstrahlung
- ionisation.

The Feynman graphs for these processes are shown in figure 2.4. The amount of energy the

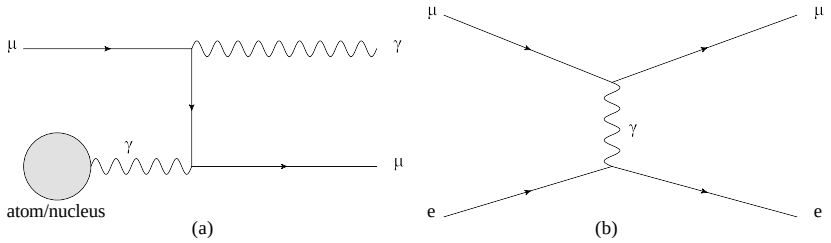

Figure 2.4: Feynman graphs for energy loss through (a) bremsstrahlung and (b) ionization. The electron is a hull electron of a material atom.

muon looses by interactions with the material it traverses depends on the passed material, the muon's velocity and the travelled distance. For ionization the energy loss per distance can be parametrized by the Bethe-Bloch-Formula 2.6:

$$-\frac{dE}{dx} = \frac{4\pi e^4}{c^2 m_e} N_A \frac{Z}{A} z^2 \frac{1}{\beta^2} \left[\frac{1}{2} \ln \frac{2 m_e c^2 \beta 2 \gamma^2 T_{max}}{I^2} - \beta^2 - \frac{\delta}{2} - \frac{C}{Z} \right] \tag{2.6}$$

The bremsstrahlung energy loss is proportional to the particle energy:

$$-\frac{dE}{dx} = \frac{1}{X_0} E \tag{2.7}$$

X_0 is the so-called radiation length, the distance after which the muon has lost all but $\frac{1}{e}$ of its initial energy. X_0 depends on the material. The critical energy E_c above which bremsstrahlung dominates the energy loss is defined as follows:

$$-\frac{dE_c}{dx}|_{ion} = -\frac{dE_c}{dx}|_{brems} \tag{2.8}$$

Some critical energies for muons in different matter are shown in table 2.5. The critical

material	$E_c(GeV)$
Si	574
Fe	355
Cu	325
Pb	140

Table 2.5: Critical energies for muons in different materials, calculated with equ. 2.9[4]. Above the critical energy, bremsstrahlung becomes the dominant process of energy loss, whereas ionization dominates the energy loss below E_c.

energy for muons in a solid with an atomic number Z can be parametrized by the following formula[4]:

$$E_c(GeV) = \frac{5700GeV}{(Z + 1.47)^{0.838}} \tag{2.9}$$

For muons, ionization energy loss is rather small for a wide range of momenta. Muons are therefore treated as minimum ionizing particles (MIPs) up to an energy of $\approx 1000GeV$.

Chapter 3

LHC and the ATLAS experiment

3.1 The Large Hadron Collider

The large hadron collider is a circular proton-proton collider located at the European Organisation for Nuclear Research (CERN) near Geneva, Switzerland. It was built in the former LEP tunnel at $70 - 100m$ below the surface and has a circumfence of $26.7km$. ALICE, CMS, LHCb and ATLAS are the four large experiments at the four beam intersection points. A schematic view is shown in figure 3.1. The LHC is designed to circulate two proton beams in opposite directions. At design parameters, each proton beam carries 2808 bunches made of 1.15×10^{11} protons. Each bunch revolves with a frequency of $11kHz$ at a bunch interval of $25ns$, leading to a bunch-crossing frequency of $40MHz$. Each proton is accelerated to an energy of $7TeV$, giving a center-of-mass (CM) energy of $14TeV$. The design luminosity will be $10^{33}cm^{-2}s^{-1}$ in the beginning, leading to an integrated luminosity of 10 fb^{-1} a year. After three years of operation the luminosity of $10^{34}cm^{-2}s^{-1}$ shall be reached, the integrated luminosity will then be $100fb^{-1}$ per year.
During the startup phase beginning in December 2009, the CM energy will be $7TeV$ [12]. The LHC will also collide lead ions, in that setup an energy of $2.76TeV$/nucleon will be reached, leading to a total CM-energy of $1.15PeV$.

The protons are injected to the LHC with an energy of $450GeV$, after having travelled through severeal pre-accelerators. The proton kinematic energy is then increased by high frequency electromagnetic field cavities. Superconducting dipole magnets with a magnetic field of $8.33T$ are used to keep the protons on their circular orbit.

3.2 The ATLAS detector

The ATLAS (A Toroidal LHC ApparatuS) detector follows the concept of a hermetic particle detector in solid angle with an onion-shell like structure. Its main components are the inner detector tracking system outside the beampipe, the electromagnetic and hadronic calorimeters and the muon spectrometer system as the outermost shell. The inner detector is penetrated by a magnetic solenoid field with a strength of $2T$, and a magnetic toroid field of $0.5 \ldots 1T$ fills the muon system. The overall length of the ATLAS detector is $44m$, it is $25m$ in diameter and weighs $\approx 7000t$. A picture is shown in figure 3.2

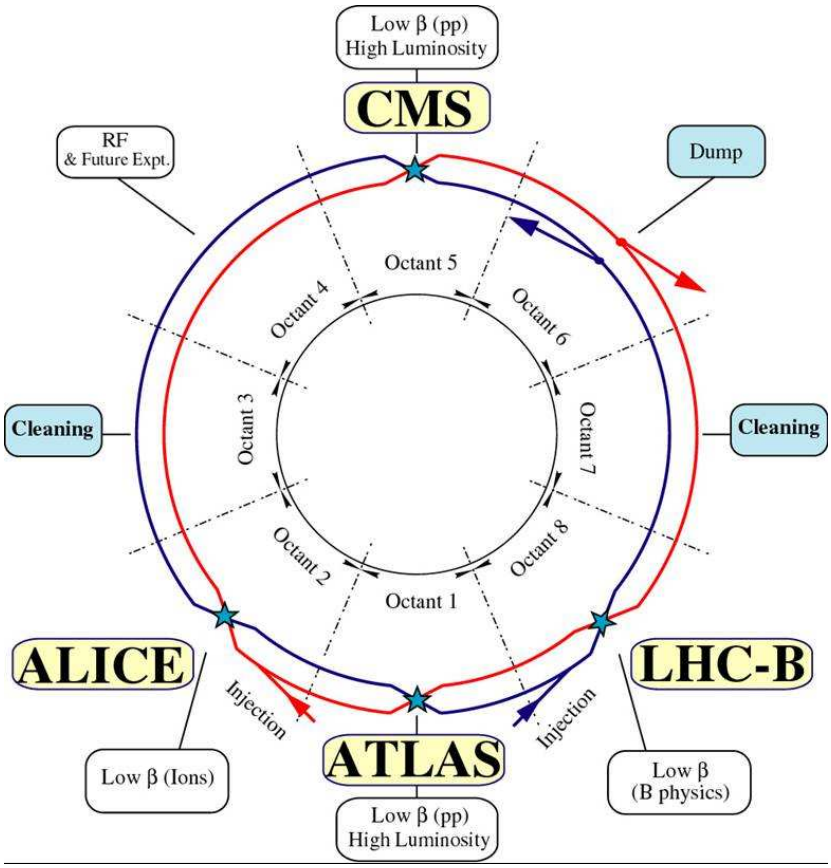

Figure 3.1: LHC schematic picture with the main experiments shown[11].

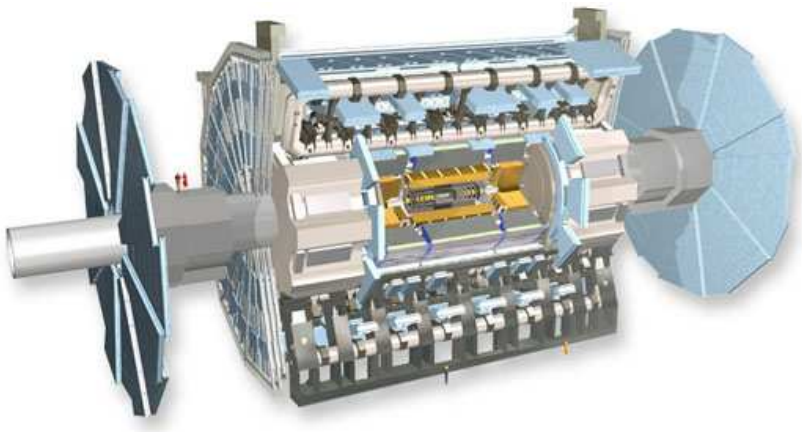

Figure 3.2: Picture of the ATLAS experiment[13].

3.2.1 The Atlas coordinate system and kinematic variables

In this section, the coordinate system and nomenclature of kinematic variables of Atlas are introduced.

The center of the cartesian coordinate system is the interaction point at the center of the ATLAS detector. The LHC beam axis points into the z - direction, x points to the center of the acceleration circle and y points to the surface. To describe the kinematics of particles in a more intuitive way, cylindrical coordinates p_T, θ and ϕ are introduced, where p_T is the transverse momentum ($p_T = \sqrt{p_x^2 + p_y^2}$) and θ and ϕ are the two angular coordinates in the $y-z$ and $x-y$ plane respectively. The advantage is the invariance of p_T under boosts in z direction. Furthermore, the pseudo-rapidity $\eta = -\ln\tan\frac{\theta}{2} = \frac{1}{2}\ln\frac{|\vec{p}|+p_z}{|\vec{p}|-p_z}$ is introduced, which is the high-relativistic limit of the rapidity $y = \frac{1}{2}\ln\frac{E+p_z}{E-p_z}$. The advantage of rapidity is its additive behavior under Lorentz transformation in z direction. A boost in z direction can be expressed as a boost matrix B depending on the rapidity y:

$$B(y) = \begin{pmatrix} \mathrm{c}(y) & 0 & 0 & -\mathrm{s}(y) \\ 0 & 1 & 0 & 0 \\ 0 & 0 & 1 & 0 \\ -\mathrm{s}(y) & 0 & 0 & \mathrm{c}(y) \end{pmatrix} \tag{3.1}$$

Two consecutive boosts $B(y_1)B(y_2)$ lead to a resulting boost:

$$\begin{aligned} B(y_1, y_2) &= \begin{pmatrix} \mathrm{c}(y_1)\mathrm{c}(y_2) + \mathrm{s}(y_1)\mathrm{s}(y_2) & 0 & 0 & -\mathrm{s}(y_1)\mathrm{c}(y_2) - \mathrm{s}(y_2)\mathrm{c}(y_1) \\ 0 & 1 & 0 & 0 \\ 0 & 0 & 1 & 0 \\ -\mathrm{s}(y_1)\mathrm{c}(y_2) - \mathrm{s}(y_2)\mathrm{c}(y_1) & 0 & 0 & \mathrm{c}(y_1)\mathrm{c}(y_2) + \mathrm{s}(y_1)\mathrm{s}(y_2) \end{pmatrix} \\ &= \begin{pmatrix} \mathrm{c}(y_1+y_2) & 0 & 0 & -\mathrm{s}(y_1+y_2) \\ 0 & 1 & 0 & 0 \\ 0 & 0 & 1 & 0 \\ -\mathrm{s}(y_1+y_2) & 0 & 0 & \mathrm{c}(y_1+y_2) \end{pmatrix} \\ &= B(y_1+y_2) \end{aligned} \tag{3.2}$$

The abbreviations s and c were used for sinh and cosh, respectively. The variables p_T, η, ϕ and E form a complete set of variables to describe the relativistic kinematics of a particle. Another kinematic variable commonly used is the invariant mass m_{inv} of two or more particles. It is defined as follows:

$$m_{inv} = \sqrt{\sum_i p_i^2}, \tag{3.3}$$

where p_i are the four-momenta of the considered particles.
The distance of two particle track vectors is expressed in ΔR:

$$\Delta R = \sqrt{(\Delta\eta)^2 + (\Delta\phi)^2} = \sqrt{(\eta_2 - \eta_1)^2 + (\phi_2 - \phi_1)^2}. \tag{3.4}$$

3.2.2 The inner detector system

The ATLAS inner detector can provide precise measurements of charged particle tracks with a high space and momentum resolution; it is capable of accurate reconstruction of the primary

and secondary vertices and must withstand the high intensity inradiation from the beam pipe. It is contained in an cylindrical envelope with a length of 3512mm and a radius of 1150mm. A picture of the Atlas inner detector system is shown in figure 3.3. The inner detector consists

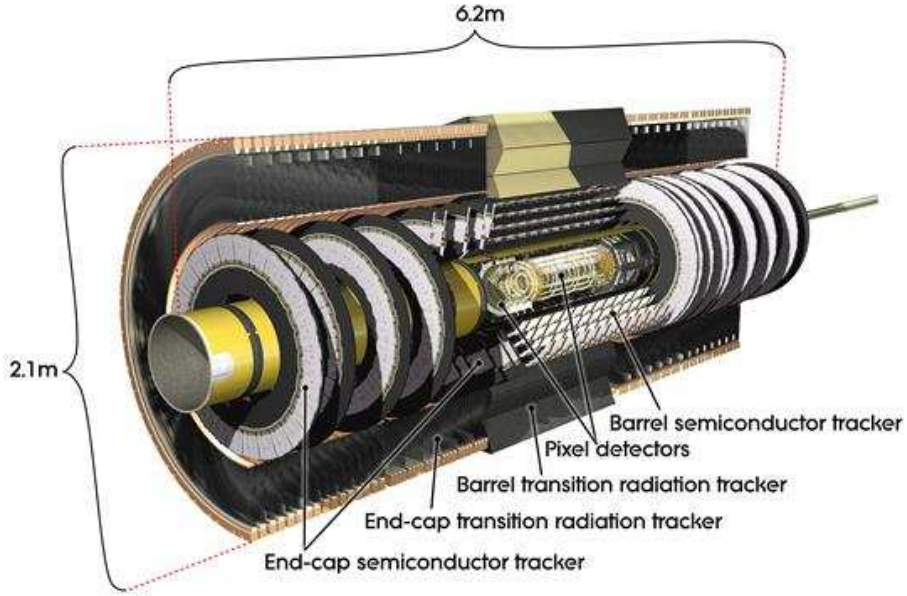

Figure 3.3: The Atlas inner detector system[14].

of three independent subdetectors:

- silicon pixel detector
- silicon microstrip tracker (SCT)
- transition radiation tracker (TRT)

The silicon pixel detector is closest to the beampipe, its semiconductive silicon pixels produce an electric signal whenever they are crossed by a charged particle due to electron-hole pair production in a depleted p-n junction. For its proximity to the beam pipe and the primary vertex, the track density is very high (several thousand particles each bunch crossing at 25 ns), therefore it needs high granularity and fast readout electronics to achieve high track recontruction efficiency.

The pixel size is $50 \times 400\mu m^2$ for 90% of the pixels, the remaining ones are $50 \times 600\mu m$ in size. Each pixel is $250\mu m$ thick. This leads to an intrinsic resolution of $10\mu m$ in $R - \phi$ direction and $115\mu m$ in z direction.

The SCT uses electron-hole production of high energetic charged particle passage as well, but within a different geometry setup. It consists of stereo pairs of silicon strips mounted at a small relative angle ($20mrad$), providing an autonomous way to measure R, ϕ and z. The strips are $285 \pm 15\mu m$ thick and have a strip pitch of $80\mu m$. They are $6cm$ long in the barrel region and $12cm$ long in the endcap region. Their intrinsic measurement accuracy is $17\mu m$ in the $R - \phi$ plane and $580\mu m$ in z direction.

The Transition radiation tracker is the outermost part of the inner detector tracking system. It is a combined detector made of polyimide drift straw detectors and transition

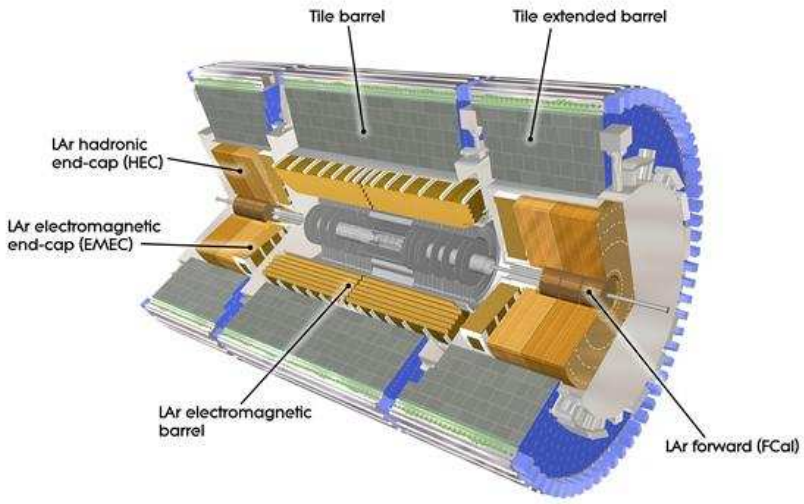

Figure 3.4: The Atlas calorimeter system with its subdetectors[15].

radiation detectors. Each of the tubes is filled with a gas mixture ($70\%Xe, 27\%CO_2, 3\%O_2$) and has a tungsten anode wire in its center. The enveloping cathode is kept under high voltage ($-1.5kV$). Whenever a charged particle crosses the gas mixture, ions and electrons are generated which drift towards the electrodes causing secondary ionisation and thus induce an electric signal on the anode wire, which is then read out by the front-end electronic boards. The drift time of the secondary electrons is used to reconstruct the track of the charged particle. The accuracy of the drift tubes is $130\mu m$. Between the tubes are several layers of different polymer foils, causing charged particles to emit transition radiation due to different dielectrical constants. This allows electron-pion discrimination due to their different γ factor.

3.2.3 The ATLAS calorimeter system

Calorimeters are used to measure the energy deposit of a massive particle or a photon. When a particle reaches the calorimeter, it interacts with the material and initiates a shower of secondary particles and thus looses energy. The electromagnetic calorimeter was designed to measure the energy of particles interacting via the electromagnetic force, namely electrons, positrons and photons. The hadronic calorimeter stops all remaining particles except muons (and neutrinos, which hardly interact at all). To maximize both energy measurement accuracy and space resolution, the calorimeters are sampled, i.e. active detector material and passive absorber/shower material are set up in turn. The ATLAS calorimeter is divided into an electromagnetic calorimeter and a hadronic calorimeter, each further segmented in barrel- and end-cap regions, see figure 3.4. The forward calorimeter is situated in the high-η-region ($3.1 < |\eta| < 4.9$).

The electromagnetic calorimeter

The electromagnetic calorimeter is a sampling calorimeter with liquid argon as active material and lead absorber plates, arranged in an accordeon-like structure, providing full ϕ coverage without geometric crack regions. The electromagnetic barrel (EMB) calorimeter covers an η range of $|\eta| < 1.475$, the electromagnetic end-cap (EMEC) covers $1.375 < |\eta| < 3.2$. The granularity of the calorimeter cells vary with η and the 3 different calorimeter layers, the $\Delta_\eta \times \Delta_\phi$ ranges are presented in table 3.1.

calorimeter part	η range	layer	granularity $\Delta_\eta \times \Delta_\phi$
EMB	$0 \ldots 1.4$	1	$0.025/8 \times 0.1$
		2	0.025×0.025
		3	0.05×0.025
	$1.4 \ldots 1.475$	1	0.025×0.1
		2	0.075×0.025
		3	0.05×0.025
EMEC	$1.375 \ldots 1.425$	1	0.05×0.1
		2	0.05×0.25
		3	0.05×0.025
	$1.425 \ldots 1.5$	1	0.025×0.1
		2	0.025×0.025
		3	0.05×0.025
	$1.5 \ldots 1.8$	1	$0.025/8 \times 0.1$
		2	0.05×0.25
		3	0.05×0.025
	$1.8 \ldots 2.0$	1	$0.025/6 \times 0.1$
		2	0.05×0.25
		3	0.05×0.025
	$2.0 \ldots 2.4$	1	$0.025/4 \times 0.1$
		2	0.05×0.25
		3	0.05×0.025
	$2.4 \ldots 2.5$	1	0.025×0.1
		2	0.05×0.25
		3	0.05×0.025

Table 3.1: Granularity of the electromagnetic calorimeter parts[13].

The performance of the electromagnetic calorimeter was studied in testbeam experiments[13]. The resolution is parametrised with a constant term and an energy-dependent term as follows:

$$\frac{\sigma_E}{E} = \frac{a}{\sqrt{E}} + b. \tag{3.5}$$

The parameters of the relative resolution of the energy measurement were determined to be

$$\frac{\sigma_E}{E} = 0.17\% + \frac{10.1\%}{\sqrt{E}}.$$

The hadronic calorimeter

The hadronic calorimeter is divided into 3 sections: the tile barrel calorimeter, the tile extended barrel calorimeter and the hadronic end-cap calorimeter (HEC). The tile calorimeters are sampling calorimeters with steel as absorber material and scintillator tiles as active detector material. A particle traversing through the steel plates induces a shower of secondary particles, which in turn produces photons in the scintillator tiles that are then converted into an electric signal and read out by photomultipliers. They cover an η range of $|\eta| < 1.7$. Testbeam studies at the SPS with isolated pions showed an η and energy dependency for the fractional resolution σ_E/E of the energy measurement in the tile calorimeter:

$$\begin{aligned}
\sigma_E/E \quad (E = 20GeV, \eta = 0.25) &= 14.2\pm0.1\% \\
\sigma_E/E \quad (E = 350GeV, \eta = 0.25) &= 6.6\pm0.1\% \\
\sigma_E/E \quad (E = 20GeV, \eta = 0.55) &= 13.0\pm0.1\% \\
\sigma_E/E \quad (E = 350GeV, \eta = 0.55) &= 5.9\pm0.1\%.
\end{aligned}$$

In the tile calorimeter, the parameters were measured to $a = 56.4 \pm 4\%$ and $b = 5.5 \pm 0.1\%$. The HEC on the other hand is a copper/liquid argon sampling calorimeter. The η coverage is $1.5 < |\eta| < 3.2$. Its performance can be characterized by the same formula (3.5), but the parameters a and b differ for different particles used in the testbeam. For electrons, a equals $21.4 \pm 0.1\%$, for pions the value goes up to $82 \ldots 85\%$. b is found to be zero within errors[13].

The forward calorimeter

The forward calorimeter (FCal) is installed in the high pseudorapidity region ($3.1 < |\eta| < 4.9$). It is a liquid argon sampling calorimeter divided into an electromagnetic part (FCal1) with copper as absorber and two hadronic parts with tungsten absorbers (FCal2, FCal3). Due to their proximity to the beam pipe, they are irradiated by a high particle flux. Thus, the liquid argon gap is smaller than in the electromagnetic calorimeters, providing a faster signal generation and higher material density. The FCal is located at a distance of $4.7m$ to the detector center. Again, the energy resolution of the FCal is different for electrons and pions. For the latter, a equals $70 \pm 0.1\%$ and b is $3.0 \pm 0.1\%$, whereas for the electrons the stochastic term a in (3.5) is $28.5 \pm 0.1\%$, and the constant term b is $3.5 \pm 0.1\%$.

3.2.4 The ATLAS Muon Spectrometer

The outermost part of the ATLAS detector is the muon spectrometer. It was designed to measure the momentum and charge of charged particles exiting the calorimeters within a range of $|\eta| < 2.7$. It consists of a barrel part, segmented into three layers, and four end-cap wheels, two on either side of the detector. In the barrel region, eight superconducting air coils generate a magnetic toroid field with a strength of $0.5T$. Two end-cap toroids, each consisting of eight coils, generate a magnetic field of $1T$ in the forward directions. The ATLAS muon system consists of four subsystems:

- monitored drift tubes (MDTs)
- cathode strip chambers (CSCs)
- resistive plate chambers (RPCs)

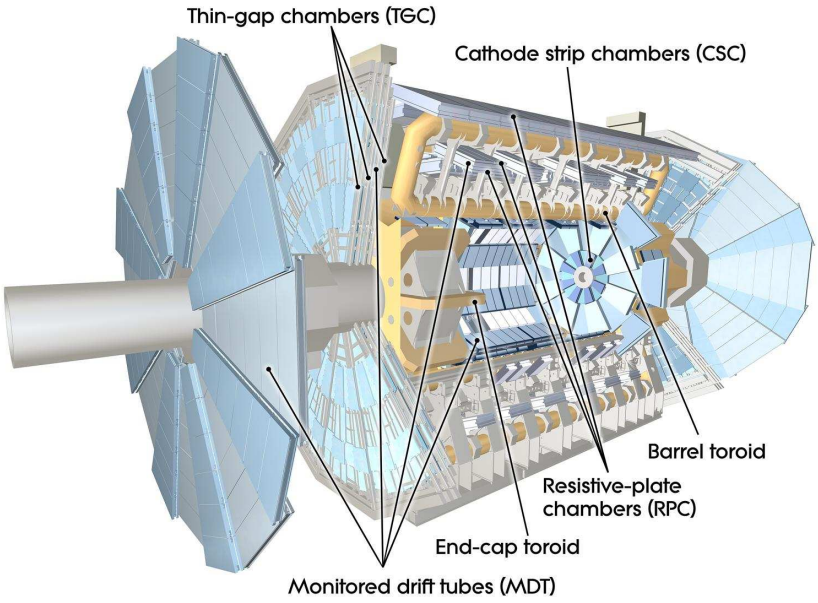

Figure 3.5: The Atlas muon spectrometer and its subdetectors[16].

- thin gap chambers (TGCs)

The monitored drift tubes and cathode strip chambers provide the precise coordinate measurement, whereas the RPCs and TGCs provide the trigger signal for this measurement. A computer-generated picture of the muon spectrometer with its subdetectors is shown in figure 3.5.

MDTs

MDTs are one of the two precision track momentum measurement detectors of the ATLAS muon spectrometer. They are arranged in three concentric layers around the beam axis in the barrel region, at radii of $5m$, $7.5m$ and $10m$. In the end-cap regions, the MDTs form large wheels perpendicular to the beam axis at distances $|z| = 7.4m$, $10.8m$, $14m$ and $21.5m$ from the interaction point. The overall η coverage is $|\eta| < 2.7$. One single drift tube chamber consists of several layers of pressurised drift tubes with a diameter of $30mm$ each, filled with an $Ar(93\%)CO_2(7\%)$ gas mixture. In the center of each tube is a tungsten-rhenium wire kept under high voltage ($3080V$). When a charged particle crosses the gas volume, it ionizes the gas atoms and produces electrons, which drift towards the anode wire producing an electric signal. The drift time of the electrones can then be resolved in a high-precicion space measurement of the track crossing the tube, taking the trigger signal of the RPCs or TGCs into account. To achieve a high resolution measurement, the drift tubes must fulfill high mechanical precicion, the wires have to be centered with an accuracy of $< 10\mu m$. Additionally the tubes arranged in a framed chamber must not be misaligned. Therefore the geometry of a chamber is monitored by four optical alignment rays (two parallel, two diagonal). Thus, geometric misalignments can be monitored and corrected later during reconstruction. The average spatial resolution per tube is $80\mu m$. By combining layers of tubes to chambers the resolution can increased to $30 \ldots 35\mu m$[13].

CSCs

The cathode strip chambers form the second precision measurement detector system in the muon spectrometer. They are used in the inner end-cap wheels at $2 < |\eta| < 2.7$ due to their higher rate capability and time resolution. There are eight small and eight large CSCs in each inner end-cap wheel. CSCs are multiwire proportional chambers with both cathodes segmented, one with the strips parallel to the wires and the other perpendicular providing two coordinate measurements. The cathode strips have a width of $1.519mm$ and $1.602mm$ in the large and small chambers, respectively. The wire spacing equals the anode-cathode-distance and has a value of $2.5mm$. The CSCs resolution is $60\mu m$ in the bending plane and 5 mm perpendicular to the bending plane.

RPCs

To complement the precision-measurement tracking chambers (MDTs and CSCs), the RPCs provide a fast trigger to deliver track information within a few tens of nanoseconds in the barrel region ($|\eta| < 1.05$). The RPC modules consist of a gas-filled ($94.7\%C_2H_2F_4, 5\%Iso - C_4H_{10}, 0.3\%SF_6$) volume between high-resistive phenolic-melaminic plates, the plate spacing is 2mm. The electric field between the plates is 4.9 kV/mm. A charged particle crossing the gas volume creates a charge avalanche due to ionization, the electric signal is read out via capacitive coupling by metallic strips mounted on the outer faces of the resistive plates. RPCs possess high detection efficiency per layer (97%) and a high rate capability of $1\frac{kHz}{cm^2}$.

TGCs

TGCs are used to provide a fast trigger and an azimuthal coordinate measurement to complemet the MDTs in the end-cap region of the muon spectrometer system, covering an eta

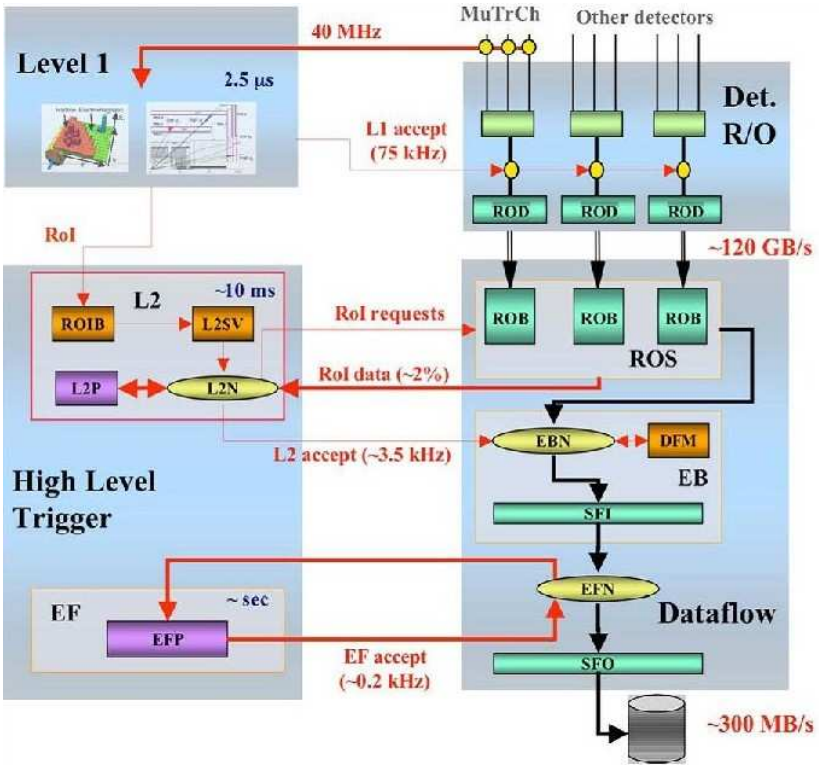

Figure 3.6: Flow chart of the ATLAS trigger system[19].

range of $1.05 < |\eta| < 2.4$. They are multi-wire proportional chambers with a wire-to-cathode distance of $1.4mm$ and a wire-to-wire distance of $1.8mm$, filled with a mixture of $CO_2(55\%)$ and $n - C_5H_{12}(45\%)$. The nominal potential on the wires is $2.9kV$. They can be used as bunch-crossing trigger, since the signal arrives within $25ns$ after the particle crossed the chamber with a probability of 99%.

3.3 ATLAS Trigger System and Event Data Model

3.3.1 Trigger System

Due to the high total cross section of inelastic proton-proton-events ($\approx 80mb$[17]) at LHC center-of-mass energy, a bunch crossing rate of $40MHz$ (provided by the LHC running at design parameters) produces 10^9 inelastic events/s at design luminosity [18]. Of these inelastic proton-proton-collisions, only a fraction contains important Standard Model and Beyond Standard Model physics events. To reduce the amount of data, a three-level trigger system has been installed: The Level-1 (L1) trigger, Level-2 (L2) trigger and the Event Filter (EF). The L1 trigger is build from custom hardware included into or parallel to the detector readout. All ATLAS subdetector systems are equipped with trigger electronics and readout devices which allows the L1 system to trigger on a wide range of relevant signatures, based on calorimetry, tracking detector and muon chamber measurements with a fast response time. The decision whether to keep an event (the L1Accept) is made within $2.5\mu s$, reducing the event rate to

$75kHz$. The L1Accept implies the construction of a ROI[1] which is fed into subsequent L2 reconstruction algorithms. The L2 software has access to detector information of higher granularity than on L1 within the ROI. The L2 trigger consists of several specialized trigger algorithms running on a CPU farm to reduce the event rate to below $3.5kHz$. The average event processing time is $40ms$. After passing the L2 trigger, the event building process takes place and an event is built from the raw data of the complete ATLAS detector, which is then passed to the Event Filter. The EF is also an algorithm-based procedure running on a processing farm. It uses the whole detector response information decide wheteher to keep the event. The processing time for a single event is approximately $4s$ [18], reducing the event rate to $200Hz$. If an event passed the EF, it is written to permanent storage.

3.3.2 ATLAS Event Data Model

The raw data generated by the ATLAS detector or simulated in Monte-Carlo event simulators is structured in a specific event data model to enable easy access to physics-relevant data and reduce the storage size required for an event. The byte-stream from the detector is first converted into a RDO (Raw Data Object), a C++ representation of the byte stream. Its size is approximately $1.2MB$/event [20]. Event physics object reconstruction algorithms use the RDO as input. The output of the event reconstruction algorithms are ESDs (Event Summary Data). They contain detailed detector information and reconstructed objects representing particle candidates with their properties. One event is $500kB$ in size at ESD level. From the ESD content, the AOD (Analysis Object Data) is derived, which is a summary of the reconstructed event sufficient for common analyses. The size of a single event is reduced to $100kB$ at AOD level[20].

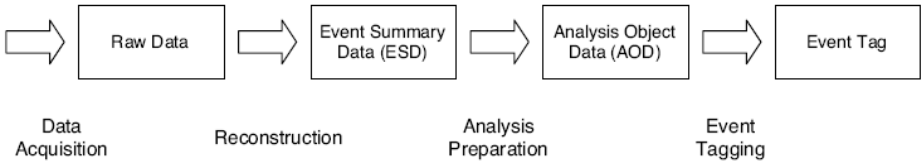

Figure 3.7: Schematic view of the ATLAS EDM data flow[20].

[1]ROI = Region-of-Interest, ATLAS fiducial detector subvolume in η and ϕ that fired the L1 trigger signal.

Chapter 4

Muon Reconstruction

At the Atlas experiment, three muon reconstruction algorithms are presently available in Atlas software to achieve high muon reconstruction efficiency and good resolution from taken data:

- standalone muon reconstruction
- combined muon reconstruction
- tag muon reconstruction

Standalone algorithms find tracks through the muon spectrometer and extrapolate them back through the rest of the detector to the beam line. Combined muon candidates are created by matching standalone muon candidates to nearby inner detector tracks, combining the measurement of these two independent detector subsystems. Tagging algorithms extrapolate inner detector tracks to the muon spectrometer and search for nearby hits. Another class of tagging methods extrapolate inner detector tracks to the calorimeter and scan for a signal of a minimum ionizing particle (MIP) in the calorimeter cells. In the Atlas computing framework Athena[21], there are two distinct families of muon reconstruction software packages with one representative implementation of each method.

	Staco family	Muid family
standalone algorithms	Muonboy	MOORE/Muid Standalone
combined algorithms	Staco	Muid Combined
tag algorithms	MuTag	MuGirl

Table 4.1: The two families of muon reconstruction algorithms and their corresponding algorithms for each class of muon reconstruction.

4.1 Standalone Muon Reconstruction

The standalone reconstruction algorithms scan for hits in each of the three layers of the muon spectrometer. At first, they build a region of interest from the trigger signals in the RPC and/or TGC (see 3.2.4). Secondly they construct so-called drift circles in the drift tubes that showed a signal. The radii of the circles are taken directly from the space information of the considered tube. The next step is the construction of tangents on the drift circles,

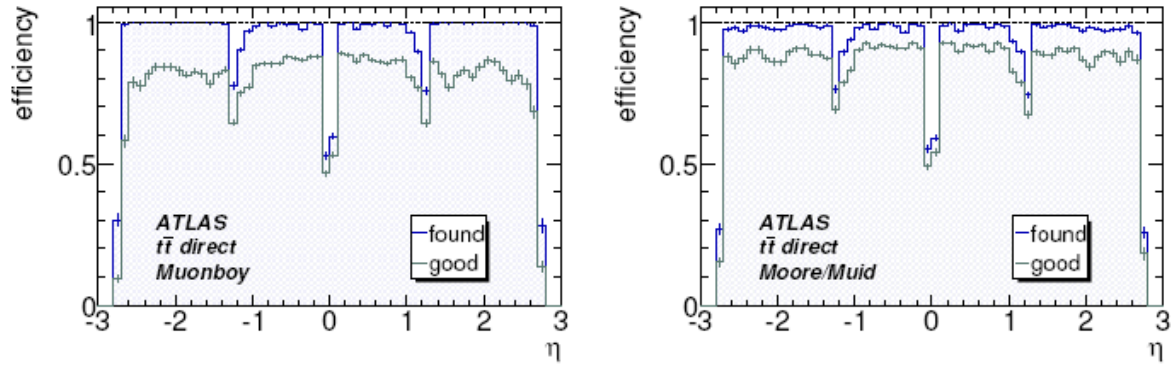

Figure 4.1: The reconstruction efficiency for the standalone muon reconstruction algorithms[13]: Muonboy (left) and MOORE/Muid (right).

always linking two of them with one tangent. From these tangents only those are kept to build a track segment that match further hit information from other drift tubes. Now a loop over all track segments is performed, combining matching segments to a road. The χ^2 of the combined match is used as a discriminating variable to reject bad roads. Finally, the remaining roads are used to build a track through the whole muon spectrometer, taking into account scattering and energy loss at the three different muon stations. In the Staco algorithm family, the standalone muon reconstruction is done by the algorithm Muonboy. MOORE (Muon Object Oriented REconstruction) and Muid-Standalone are the corresponding algorithms in the Muid algorithm family. The performance of the standalone algorithms is mainly affected by the detector coverage. The reconstruction efficiency decreases significantly at the gaps in the muon spectrometer. These are the service gap in the $|\eta| = 0$ region and the gap in the transition region between barrel and end-cap muon spectrometer at $1.2 < |\eta| < 1.4$. Standalone muon performance studies[13] have been done on a $t\bar{t}$-sample in which there is at least one lepton. The results are presented in figure 4.1.

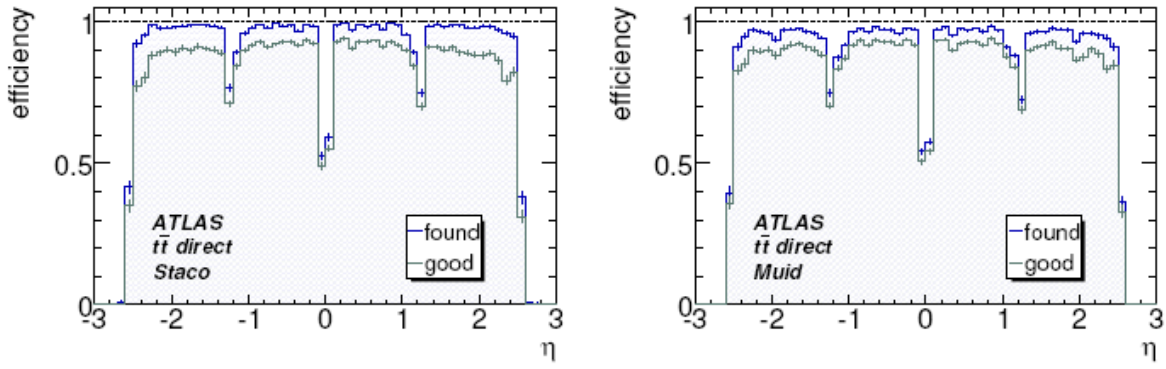

Figure 4.2: The reconstruction efficiency for the combined muon reconstruction algorithms[13]: Staco (left) and Muid (right).

4.2 Combined Muon Reconstruction

Both muon combination algorithms, Staco and Muid, use the standalone muon tracks and combine them with inner detector tracks to create a combined muon candidate. Muid combines the inner detector track vector with the information of the muon spectrometer track, taking into account multiple scattering and energy loss in the calorimeter layer and the bending effect of the magnetic field. Staco statistically combines the standalone track parameters and covariance matrices, extrapolated back through the calorimeter to the inner detector, and the track parameters and covariance matrices measured in the inner detector. The combined track vector T is calculated as:

$$T = (C_{ID}^{-1} + C_{MS}^{-1})^{-1}(C_{ID}^{-1}T_{ID} + C_{MS}^{-1}T_{MS}) \tag{4.1}$$

where C_{ID} and C_{MS} are the inner detector and muon spectrometer covariance matrices, and T_{ID} and T_{MS} are the inner detector and muon spectrometer track vectors, respectively. The match-χ^2, defined as follows:

$$\chi^2_{match} = (T_{MS} - T_{ID})^T(C_{ID} + C_{MS})^{-1}(T_{MS} - T_{ID}) \tag{4.2}$$

provides an important measurement of the combination quality. Hence, it relies on the detector alignment, so its usage for first data is not recommended. The combined muon performance has been studied [13] on the same $t\bar{t}$-sample as the standalone muon reconstruction algorithms. The results are as shown in figure 4.2. Again the effect of the service gap and transition region is clearly visible.

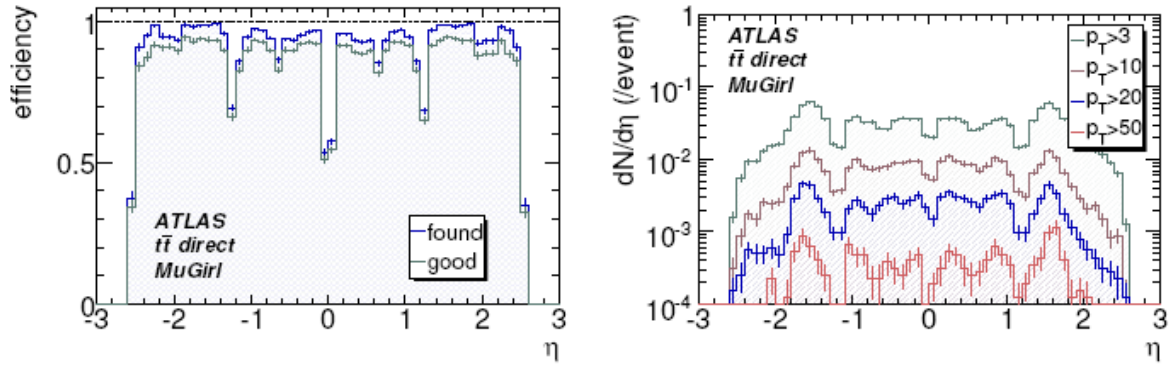

Figure 4.3: The reconstruction efficiency (left) and fake rate (right) for the tagged muon reconstruction algorithm MuGirl[13].

The families and the outcoming muon collections are named after the combined muon algorithm, the Staco family and the Muid family, respectively. The current default for physics analyses is the Staco muon collection, which was also used in this thesis' studies.

4.3 Tagged Muon Reconstruction

The muon tagging algorithms MuTag (Staco family) and MuGirl (Muid family) complement the results of the standalone- and combined muon reconstruction algorithms: they extrapolate inner detector tracks with sufficient momentum through the calorimeter into the muon spectrometer and search for nearby hits. MuTag then performs a χ^2 match of the muon spectrometer segment and the extrapolated track as a discriminating variable, whereas MuGirl uses an artificial neural network to define a discriminant. In both cases the inner detector track is tagged as a muon candidate track if the track segment is sufficiently close to the expected track position from the extrapolation. The performance of MuGirl is lower than that of standalone or combined algorithms, with a lower efficiency and higher fake rate, shown in figure 4.3. MuTag is only used to complement the Staco family muon reconstruction. It only considers inner detector tracks and muon spectrometer track segments that were not used by Muonboy or Staco themselves, therefore comparative efficiencies and fake rates have not been determined.

Chapter 5

Z^0+Jets Reconstruction

5.1 Motivation

Studying Z^0 events at the LHC possesses fundamental importance in several ways. For starters, Z^0 production can be a stringent test of QCD, since the calculation of higher order corrections to Z^0+jets final states cross sections is very advanced with a theoretical uncertainity $< 1\%$ (see section 2.3). Moreover the leptonic final states $Z^0 \rightarrow ee$ and $Z^0 \rightarrow \mu\mu$ can be fully reconstructed and thus allow precise measurement of p_T and η dependency of the cross section, giving more insights on the parton distributuion functions of the proton. In principle this will improve every measurement at the LHC, since the PDF uncertainities are limiting factors in LHC physics calculations. Furthermore the Z^0 properties have been precisely studied at LEP[22]. Exploiting its mass, width and leptonic branching ratios can lead to a better detector understanding in terms of energy and momentum scale and lepton identification efficiency. At last various fundamental electroweak parameters can be accessed through Z^0 final states, for example $\sin^2\theta_W$ (via Z^0 forward-backward asymmetry) and lepton universality.

5.1.1 $Z^0 \rightarrow \mu\mu$ + jets properties

Selection and reconstruction of $Z^0 \rightarrow \mu\mu$ + Jets events uses the expected properties of the decay muons. Due to momentum conservation, the produced Z^0 boson must balance the summed transverse momenta of the produced hadronic jets, which constraints the recoil of the Z^0 in the transverse plane. The momentum parallel to the beam axis cannot be measured, since the interacting partons producing the Z^0 carry only an experimentally unknown longitudinal fraction of the proton's momentum.

The Z^0 rapidity distribution for the Drell-Yan process including higher order corrections described in 2.3.1 is shown in figure 5.1. Z^0 bosons are thus mainly produced in forward or backward direction. This can be understood by taking into account that the involved antiquark carries a much lower fraction of the proton's momentum than the quark, so the center of mass of the two involved quarks is moving in either z direction in the lab frame. The same applies for the higher order processes involving a quark and a gluon in the initial state.

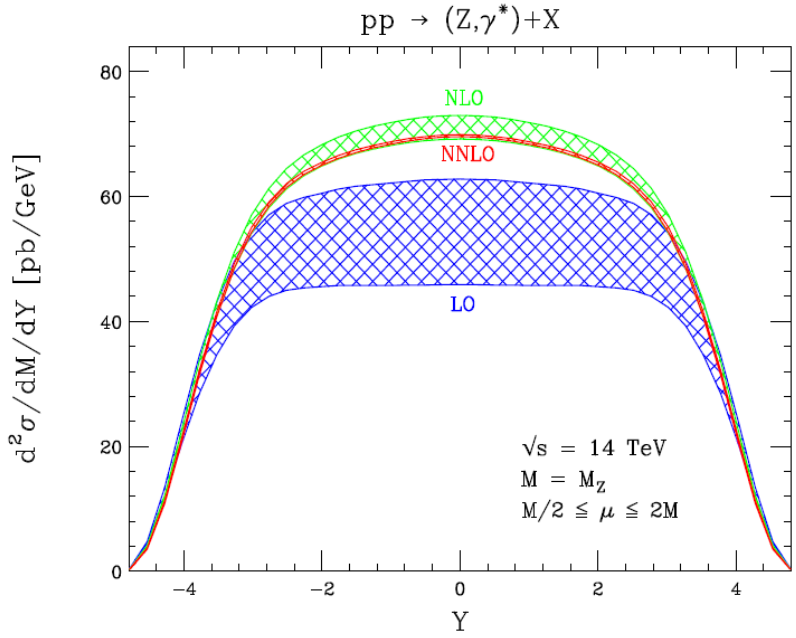

Figure 5.1: The calculated rapidity distribution of Z^0 bosons at the LHC. The bands show the theoretic uncertainties of leading order, next-to-leading order and next-to-next-to-leading order calculations[23].

5.1.2 Muon Properties

Muons from Z^0 decays

In the Z^0 rest frame, the two decay muons are produced back-to-back and carry away all of the Z^0 mass and energy in their momentum. When the system is boosted to the lab frame, the angle between the muons becomes smaller, depending on the velocity and direction of the Z^0 boson. What is expeced from muonic Z^0 decays at ATLAS are two oppositely charged high energetic muons with a substantial transverse momentum p_T in most of the cases, emerging from one vertex (the Z^0 decay vertex).

Muons from background processes to Z^0 production

Muons are also found among the decay products of other particles (besides others not listed here):

- W bosons
- b-quarks
- hadrons in jets
- $t\bar{t}$ events

The W boson's mass is $80.4GeV$, the decay muon's energy and momentum is comparable to those from a Z^0 decay. The muon from a W decay is accompanied by a neutrino, not a second muon of opposite charge, which helps to distinguish between these channels.

Another source of muons are decays of mesons containing b-quarks. Two muon production modi are known: the Υ meson can decay directly into two muons, the Feynman graph is shown in figure 5.2.The branching fraction of this decay is $\approx 2.5\%$[4]. This decay channel is analogous

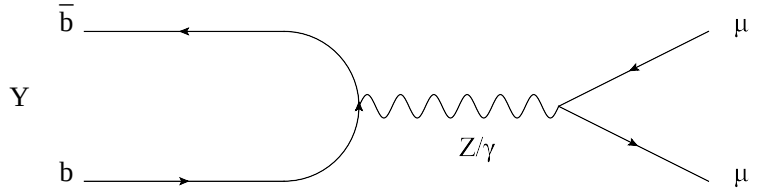

Figure 5.2: Feynman graph for the decay of the Υ meson into two muons.

to the Z^0 decay, except that the $\Upsilon's$ mass is much lower ($9.46 \ldots 10.58 GeV$[4], depending on the spin state of the Υ) and thus the muons' energies are lower than in the Z^0 decay products. Muons are also found among the decay chains of other B mesons ($B^{\pm}$, B^0, $\overline{B^0}$)(see figure 5.3). In this case, the decay muon is accompanied by other decay products caused by the boost of the decaying B meson. Again, the muon's energy is substantially lower than the energy of Z^0 decay products. Muons can also be produced by weak decays of other hadronic particles

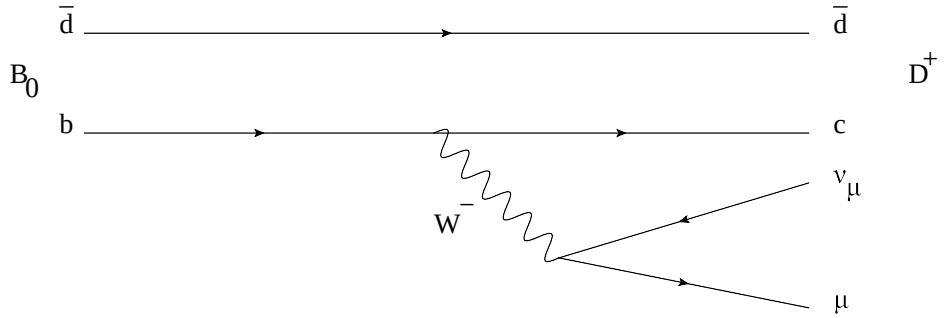

Figure 5.3: Feynman graph for the decay of a neutral B meson into a charged D meson, a muon and a muon-antineutrino.

in jets. These include decays of $\pi^{\pm}$, $K^{\pm}$ and cascading decays of charmed mesons. Again, in contrast to muons from a Z^0 decay, these muons are produced in the hadronic environment of a particle jet and are thus accompanied by a variety of other particles. Furthermore, they tend to be produced off the primary vertex due to the lifetime of the decaying hadrons.

In $t\bar{t}$ events muons can either originate from W decays or from decays of B mesons. If both W bosons decay leptonically to $\mu\nu$, the signature is quite similar to a $Z^0 \rightarrow \mu\mu$ + jets event. A discriminating signature is that the energies of the two muons is not correlated.

5.1.3 Isolation criteria

To distinguish between muons originating from the decay of a Z^0 boson and those from weak decays within hadronic jets, isolation criteria are established. There are two qualitatively different approaches in defining isolation criteria:

- track based isolation criteria
- calorimeter based isolation criteria.

Track based isolation criteria use the inner detector tracking information. Since isolated muons tend to have a low number of other tracks around them (or none at all), an useful discriminating variable is the number of tracks in an $\eta - \phi$-cone (see equation 3.4) around the muon candidate track. There are other ways to create a track-based isolation criterion than simply counting the number of tracks. The sum of the tracks' transverse momenta can be used, and/or a weight can be introduced depending on the ΔR distance of the tracks to the muon track.

Calorimeter based isolation criteria use the energy measurement matched to a muon candidate in the ATLAS calorimeter system. A muon can be considered as a minimum ionizing particle (MIP) up to an energy range of $\approx 1000 GeV$ (see section 2.3.3), so its energy loss in the calorimeter is rather small. If there is a significantly higher energy deposit in the calorimeter around the muon track, this was due to other particles entering the calorimeter, and thus the muon was not isolated. Therefore, the deposited energy in an $\eta - \phi$ - cone around a muon candidate track is used as discriminating variable. Furthermore, an inner cone is defined and the energy deposited there is subtracted to account for the energy loss of the muon itself. There are also more subtle ways to distinguish between isolated and non-isolated muons using the energy deposit, for example weighting the energy with the muon's transverse momentum.

These two different approaches can be combined to create more powerful muon isolation criteria. For ATLAS analyses, a common muon isolation criterion has been defined as follows[13]:

- number of tracks in cone $0.2 < 2$
- energy deposit in the electromagnetic calorimeter $< 2GeV$, inner cone: 0.075, outer cone 0.15
- energy deposit in the hadronic calorimeter $< 10GeV$, inner cone: 0.15, outer cone 0.30.

Simulation studies [13] have shown the following properties of this criterion:

- efficiency of tagging the muon from $(W \rightarrow \mu\nu)$ as isolated: 80%
- efficiency of tagging non-isolated muons from b-quark decays: 0.2%.

Chapter 6

Muon Isolation Efficiency Estimation

6.1 Data samples

To obtain reasonable isolation efficiencies, this study has been done on a mixture of data samples resembling the expected event environment during data taking at the ATLAS detector. Signal and background datasamples were selected to cover as much phase space as possible, and to consider all possible final state background processes. All simulated events were generated with a eneter-of-mass-energy of $10TeV$. As $Z^0 \rightarrow \mu\mu$ signal samples were selected:

- mc08.107660.AlpgenJimmyZmumuNp0_pt20r696
- mc08.107661.AlpgenJimmyZmumuNp1_pt20r696
- mc08.107662.AlpgenJimmyZmumuNp2_pt20r696.

These are $Z^0 \rightarrow \mu\mu + Jets$ events generated by the Alpgen[24] Monte Carlo generator. The tag "NpX_pt20" notes the number of generated partons with a transverse momentum of at least 20 GeV. This is strongly correlated to the number of jets in the event, although this can differ due to gluon radiation after the simulated hard process. The number after "mc08" is the RunNumber, an useful identifier of the data sample in combination with the reconstruction tag "r696".

The background samples can be divided into three groups, presented in table 6.1. On the QCD samples a muon filter was applied during simulation. They contain at least one muon per event. The tags "$J0 \ldots J5$" refer to the transferred momentum (Q^2) of the simulated hard scattering process (see table 6.2). This value is correlated to the energy of the most energetic particle jet in the event. The samples with run number 107340 and 107341 contain b-quarks, which can be a source of non-isolated muons as described in section 5.1.2.

These samples all contain a different number of single events, and each of the samples simulates a physical process with a distinctive cross section. To compare event numbers and to be able to use them parallel to each other, they need to be normalized to a particular integrated luminosity $\int \mathcal{L}$ (see equation 2.3). In this analysis, $\int \mathcal{L}$ was chosen to $10pb^{-1}$, which corresponds to several days of data taking during LHC startup phase[25]. The event

background type	1—c—sample
$t\bar{t}$ events	mc08.105200.T1_McAtNlo_Jimmyr696
$W \rightarrow \mu\nu$+Jets events	mc08.107691.AlpgenJimmyWmunuNp1_pt20r635
	mc08.107692.AlpgenJimmyWmunuNp2_pt20r635
QCD events	mc08.107340.AlpgenQcdbbJ2Np0_TOPfiltmu_pt20r635
	mc08.107341.AlpgenQcdbbJ2Np1_TOPfiltmu_pt20r696
	mc08.108818.AlpgenQcdJ2Np2_TOPfiltmu_pt20r635
	mc08.108824.AlpgenQcdJ3Np3_TOPfiltmu_pt20tid068950
	mc08.109276.J0_pythia_jetjet_1muontid064626
	mc08.109277.J1_pythia_jetjet_1muontid068975
	mc08.109278.J2_pythia_jetjet_1muontid068974
	mc08.109279.J3_pythia_jetjet_1muontid068976
	mc08.109280.J4_pythia_jetjet_1muontid046362
	mc08.109281.J5_pythia_jetjet_1muontid046364

Table 6.1: Background samples used in this analysis.

J value	range of Q^2(GeV)
J0	8...17
J1	17...35
J2	35...70
J3	70...140
J4	140...280
J5	280...560

Table 6.2: J values and the corresponding Q^2 of the hard process.

weight w is calculated in the following way:

$$w = \frac{\sigma \cdot \mathcal{L} \cdot \epsilon}{N} \tag{6.1}$$

Here, σ denotes the cross section of the process in the sample. ϵ is a filter efficiency ensuring correct normalisation of the respective sample's contribution, if filters were applied at event generation. N equals the number of events in the considered data sample. The properties of each datasample used in this analysis are listed in table 6.3.

RunNumber		σ (pb)	ϵ	N_{EV}	weight w
$Z \to \mu\mu$	107660	9.002×10^{2}	1	28000	0.3215
+Jets	107661	2.052×10^{2}	1	6987	0.2937
(signal)	107662	6.94×10^{1}	1	20862	0.0333
$W \to \mu\nu$	107691	2.156×10^{3}	1	246970	0.0873
+Jets	107692	6.823×10^{2}	1	594733	0.0115
$t\bar{t}$	105200	3.736×10^{2}	5.43×10^{-1}	151657	0.0135
QCD	107340	9.119×10^{3}	5.28×10^{-2}	91398	0.0527
	107341	7.708×10^{3}	3.17×10^{-2}	9778	0.2497
	108818	4.638×10^{4}	1.21×10^{-3}	44702	0.0126
	108824	6.903×10^{3}	3.71×10^{-3}	7250	0.0353
	109276	1.17×10^{10}	5.28×10^{-5}	73354	84.216
	109277	8.668×10^{8}	1.02×10^{-3}	18000	491.19
	109278	5.601×10^{7}	4.59×10^{-3}	18958	135.61
	109279	3.28×10^{6}	1.27×10^{-2}	23958	17.387
	109280	1.516×10^{5}	2.04×10^{-2}	19980	1.5479
	109281	5.122×10^{3}	2.99×10^{-2}	3500	0.4376

Table 6.3: Properties of the used datasamples. Floating point numbers are rounded to the last digit.

6.2 $Z^0 \to \mu\mu$ selection with the "tag and probe" method

The efficiency of an isolation criterion is the fraction of real isolated muons that passed the criterion divided by all real isolated muons. Without knowing whether a reconstructed muon candidate seen in data was a real isolated muon, the term "isolated" is replaced with "hard process", since muons which emerged directly from the hard process tend to be isolated. Therefore the definition of a muon isolation efficiency in this context is:

$$\epsilon = \frac{\#\text{ of hard process muons that passed isolation criterion}}{\#\text{ of hard process muons}} \tag{6.2}$$

Still a subset of data in which every muon candidate originated from the hard process has to be selected. Because of its clean experimental signature, the $Z^0 \to \mu\mu$ channel was chosen.

A method very well suited to determine muon related efficinecies from first data is the tag and probe approach. This ansatz selects muon candidates following hard criteria, called tag muons, and hence combines their recuonstructed kinematic properties with the remeining muon candidates in the event. If both fulfill a minimum requirement of cuts and the Z^0

invariant mass condition, the tag and probe candidates can be used to define a distinct statistical sample with known properties. Stringent cuts are applied to the tag muon to ensure high purity. The tag muon cuts used in this analysis are the following:

- $p_T > 15GeV$
- $0.1 \leq \eta \leq 2.5$
- isBestMatch = true
- $\frac{\chi^2}{DoF} \leq 8$ (see equation 4.2)
- passed CSC muon isolation criterion (see section 5.1.3)

The Z^0 subsample selection is carried out as follows: First, the event is searched for two oppositely charged Staco muon candidates to build muon candidate pairs. Now it is checked whether the muon candidate pair contains at least one tag muon candidate. If there are more than one muon candidate pair per event left, the one with the highest scalar transverse momentum sum of its components is selected. The final selection requirement is a mass window cut on the muon candidate pair's invariant mass: $71GeV \leq m_{\mu\mu} \leq 111GeV$

To check whether the $Z^0 \rightarrow \mu\mu$ sample selection was successful, a truth matching method has been developed for the muon pair. Since different Monte-Carlo generators were used for different data samples, the truth matching method had to be generator-independent.

At first, the algorithm loops over all truth particles and selects muons or antimuons, respectively. When a muon is found, its production vertex is retrieved, together with all other particles that were produced at this vertex. If there is another (anti-)muon or a (anti-)muon neutrino, the invariant mass of the two particles is calculated from their true (generator-level) Lorentz vectors (see section 3.2.1). If the invariant mass exceeds a threshold of $60GeV$, the primary muon is considered as "truth isolated". To ensure that these truth muons correspond to a reconstructed detector object, a truth-to-reconstruction matching is performed. If a Staco reconstructed muon object exists with a maximum ΔR-distance of 0.1, the truth muon's barcode is stored as a unique identifier.

On the reconstruction side, every muon candidate is assigned the tag "truly isolated" if it was matched to a truth muon whose barcode has been stored.

With these classifications the quality of the sample selection can be quantified as purity p in:

$$p = \frac{N_{\mu\mu,true\ isolated}}{N_{\mu\mu,selected}} \tag{6.3}$$

Here, $N_{\mu\mu,true\ isolated}$ is the number of selected muon pairs where both muons have been assigned "truly isolated", and $N_{\mu\mu,selected}$ is the total number of selected muon pairs. Table 6.4 shows the cut flow and purity of the $Z^0 \rightarrow \mu\mu$ sample selection. The number of muon pairs may be fractional, this is due to the event normalization to $10pb^{-1}$ integrated luminosity.

The final selection purity is[1]:

$$p = (90.99 \underbrace{^{+0.37}_{-0.36}}_{\Delta p_{bin}} \underbrace{^{+6.18}_{-18.19}}_{\Delta p_{poi}})\% \tag{6.4}$$

[1]The errors consist of two parts: a binomial part Δp_{bin} calculated as described in [26], and a Poissonian estimate Δp_{poi} to cover the impact of the high-weight QCD background event.

This purity is substantially below the target value of 100%. The reason can easily be found by examining the corresponding distributions of the $m_{\mu\mu}$ invariant mass spectrum shown in figure 6.1. One single QCD background event with a weight close to 500 remains in the selected

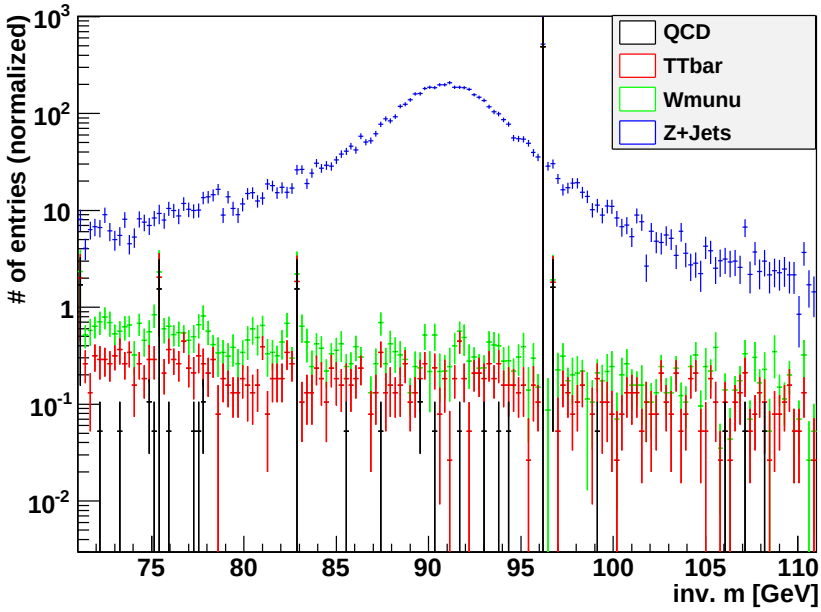

Figure 6.1: The invariant mass spectrum of the muon candidate pairs after the $Z^0 \rightarrow \mu\mu$ selection via tag and probe.

sample and substantially lowers the purity of the selection. This single event is also the main contribution to the purity error. To resolve this issue, an increased number of events in this particular background sample would be required, which was not available for this analysis.

selection	$\mu\mu$ pairs	true $Z \rightarrow \mu\mu$ pairs	purity (%)
opposite charge	1.282×10^6	6.469×10^3	0.50
tag muon requirement	6.847×10^4	6.159×10^3	8.99
maximum $\sum \lvert p_T \rvert$	6.459×10^4	6.046×10^3	9.36
M_Z window	6.152×10^3	5.598×10^3	90.99

Table 6.4: Cut flow of the $Z^0 \rightarrow \mu\mu$ sample selection.

6.3 Implemetation of Isolation Criteria

Once the $Z^0 \rightarrow \mu\mu$ selection has been performed, the isolation efficiency determination can be executed. Three different types of isolation criteria were applied to the probe muon of the muon pair:

1. etcone: $\sum E_T(cone\ X) - \sum E_T(cone\ 0.05) \leq$ cut value
2. etcone/$p_{T,\mu}$: $\frac{\sum E_T(cone\ X) - \sum E_T(cone\ 0.05)}{p_{T,\mu}\text{candidate}} \leq$ cut value
3. nucone: (inner detector tracks)$|_{cone\ X} \leq$ cut value

The first two criteria are calorimeter-based isolation criteria, while the last one is track-based. The cone sizes *cone X* were chosen in a range from $0.05 \ldots 0.45$ in steps of 0.05 around the muon candidate track. For the track isolation criterion *nucone*, the muon candidate track itself was subtracted from the number of inner detector tracks in the respective cone. The implementation of all three criteria includes two basic steps:

1. extraction of necessary data from ESD (see section 3.3.2)
2. specific implementation and application the separate analysis code

In the first step all necessary information is extracted from the ESD. In particular, a loop is executed over all Staco muon candidates. The muon candidate kinematic variables p_T, η, ϕ and E are stored in the n-tuple. Additional relevant muon properties include quality variables, such as *bestMatch*, *isCombined*, *isHighPt*, χ^2/DoF[27] and the barcode of the truth muon the reconstructed muon candidate is matched to (see section 6.2). For every muon candidate three different tools are called to extract information from the ESD. The *TrackIsolationTool*[28] is used for two purposes: given the range of cone sizes, it returns both the number of tracks around the muon candidate track in each cone and the calorimeter energy summed over all layers in each cone. To account for the different calorimeter layers (see 3.2.3) and to cross-check the results of the *TrackIsolationTool*, the *TrackInCaloTool*[28] is called afterwards. It not only returns the summed energy in each given cone, but also a list of individual calorimeter cells that were used in the energy summation. For each of the cells in the cell list, the *CaloNoiseTool*[29] is then called to retrieve the electronic noise of the calorimeter cell. The electronic noise of all cells in one calorimeter layer[2] is summed in quadrature for each cone to get an estimate for the uncertainity of the energy measurement.

[2]In this analysis the calorimeter layers are grouped in 4 parts: PS is the presampler, EM includes the electromagnetic barrel and end-cap calorimeters, TILE are the hadronic tile calorimeter layers and HEC refers to the hadronic endcap calorimeters.

Chapter 7

Results

7.1 Isolation Efficiencies

All three isolation criteria described in section 6.3 were applied to all probe muons of the selected $Z^0 \rightarrow \mu\mu$ subsample with the following cut values:

- etcone: $0.5 \ldots 4.5 GeV$ in steps of $0.5 GeV$
- etcone/$p_{T,\mu}$: $0 \ldots 0.6$ in steps of 0.06
- nucone: $0 \ldots 7$ tracks in steps of 1 track.

For each combination of cut value and cone size, the isolation efficiency was then calculated analogous to equation 6.2:

$$\epsilon = \frac{\text{\# of probe muons that passed isolation criterion}}{\text{\# of probe muons}} \tag{7.1}$$

Assuming the application of an isolation criterion on a set of probe muon candidates is a binomial statistic process (a muon candidate can either pass the criterion or not), binomial errors were calculated as described in [26]. As already mentioned in section 6.2, the impurity of the sample is problematic when calculating the isolation efficiencies. Since the single QCD background event has such a high weight, the isolation efficiency for any criterion drops by ≈ 0.08 when this single event does not fulfill this criterion and therefore does no longer contribute to the nominator in equation 7.1. A further treatment of this influence was not possible in this analysis, so every calculated isolation efficiency is affected by a total uncertainty of ≈ 0.08 due to the impurity of the reference sample.

7.1.1 Calorimeter Isolation Efficiencies

The determined calorimeter isolation efficiencies are presented in figure 7.1 As an example, the calorimeter isolation efficiencies for a fixed cut value of $1 GeV$ are presented in table 7.1. The overall shape of the efficiency distribution can be described as follows: The looser the cut (i.e. the greater the cut value), the higher the efficiency, and the bigger the cone, the lower the efficiency. This is a completely expected behavior. With a rising cone size, the energy measurement of more calorimeter cells is used and the probability that a particular muon candidate does no longer fulfill the isolation criterion increases. For increasing cut values, the

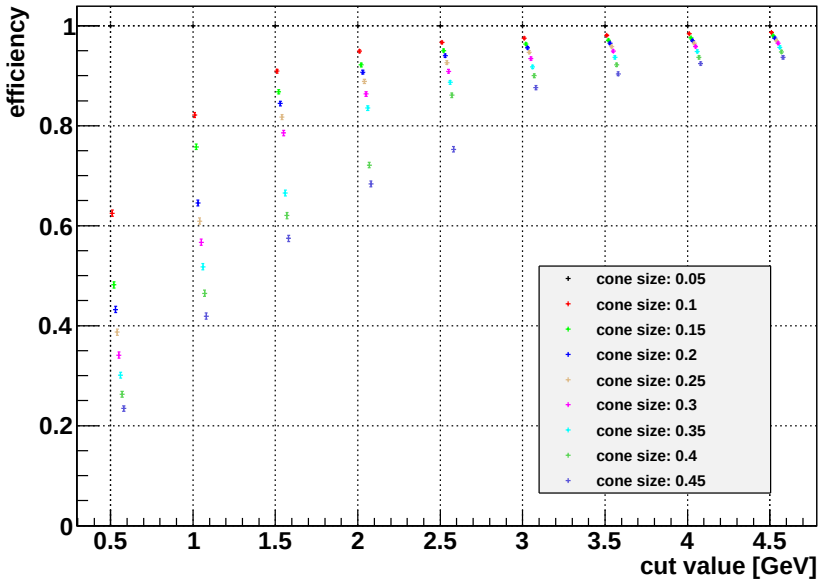

Figure 7.1: Calorimeter isolation efficiencies determined as discussed in section 7.1. The different cut values are on the x axis, the value of the efficiency are an the y axis. The different cone sizes are color-coded. The data points are slightly shifted to distinguish overlapping entries. Only statistic binomial errors are shown.

etcone criterion		cut value = $1GeV$
cone size	efficiency $\epsilon(\%)$	$\Delta\epsilon_{bin}(\%)$
0.1	82.11	± 0.49
0.15	75.76	$^{+0.54}_{-0.55}$
0.2	64.55	± 0.61
0.25	60.89	± 0.62
0.3	56.67	$^{+0.64}_{-0.62}$
0.35	51.78	$^{+0.65}_{-0.63}$
0.4	46.46	$^{+0.64}_{-0.63}$
0.45	41.90	$^{+0.64}_{-0.62}$

Table 7.1: Isolation Efficiencies and their binomial errors.

chance that a muon candidate passes the cut increases, therefore the isolation efficiency rises due to the increasing nominator in equation 7.1.

As discussed in section 7.1, the influence of the single high weight QCD background event is clearly visible in the "gaps" and "steps" of the isolation efficiencies.

The gaps occur if the QCD event passes the respective cut for one cone size, and does not fulfill the criterion for a bigger cone size. The steps mark the transition when the QCD event does not fulfill one particular cut for a fixed cone size, but passes a looser cut for the same cone size.

7.1.2 Track Isolation Efficiencies

The track isolation efficiencies are shown in figure 7.2 Similarly to the calorimeter isolation

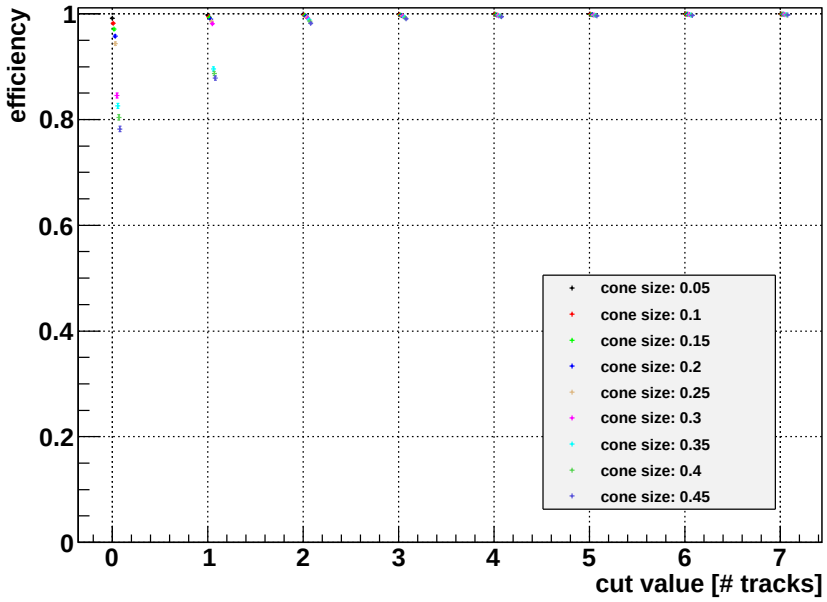

Figure 7.2: The calculated track isolation efficiencies dependent on the respective cut value (track number cut). The structure and color coding is the same as for figure 7.1.

efficiency distribution, the track isolation efficiencies show the expected behavior: The bigger the cone, the more inner detector tracks are possibly collected around the muon candidate track, resulting in a decreasing efficiency. And the higher the cut value, the more muon candidates pass the respective cut and the isolation efficiency rises. Again, the impact of the single QCD background event is obvious. The overall efficiency is higher than for the calorimeter isolation criteria.

7.1.3 $E_T/p_{t,\mu}$ Isolation Efficiencies

The $E_T/p_{t,\mu}$ isolation efficiencies are shown in figure 7.3 Again the overall shape of the isolation

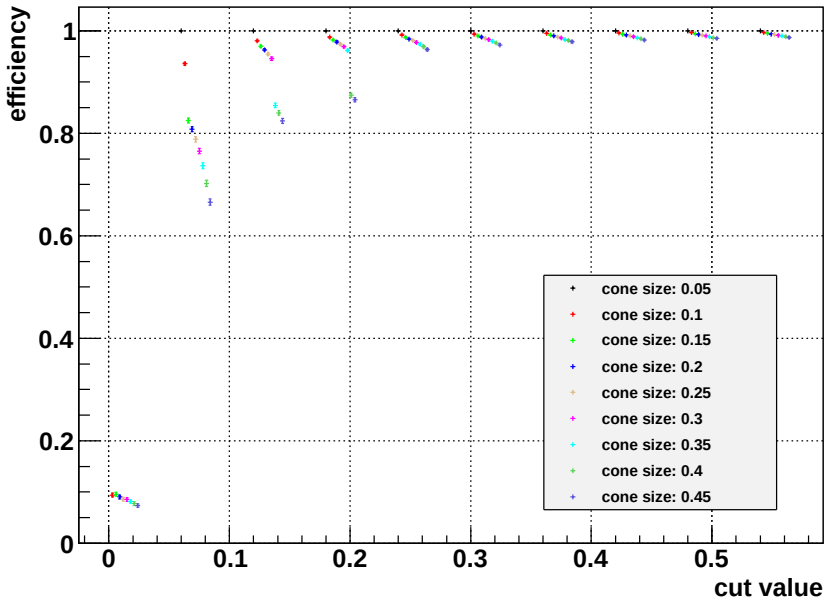

Figure 7.3: The isolation efficiencies obtained from the $E_T/p_{t,\mu}$ isolation criterion as a function of the respective cut value.

efficiency distribution is as expected. The greater the cone around the muon candidate, the more energy is eventually summed up and the efficiency decreases. On the other side more muon candidates possibly pass a higher cut value and therefore the isolation efficiency increases.
The low efficiency in the first bin is due to the cut value of 0, which can hardly be fulfilled by any probe muon candidate. Only if no additional energy was deposited around the muon candidate, the nominator in the definition of the criterion (see section 6.3) can be zero and the muon candidate passes the cut. As stated before, the influence of the QCD background event is clearly visible. Depending on the cut value, the $E_T/p_{t,\mu}$ isolation criterion shows a more stable behaviour than the pure calorimeter isolation criterion, whereas the track isolation criterion is clearly more efficient.

7.2 Systematic Uncertainities

The systematic impact of measurement uncertainities on the isolation efficiencies have to be taken into account to obtain reasonable results. Two types of uncertainities were investigated:

- energy measurement: electronic calorimeter noise. Necessary information is directly obtained from the ESD (see section 6.3).
- track number measurement: track reconstruction efficiency. The track reconstruction efficiency is obtained from [13] and is set to 99%.

For the impact of the uncertainity of the energy measurement a *Gaussian approach* was used. The measured energy E in each calorimeter cell is assumed to be Gaussian distributed with a mean of E and a width σ_E that equals the electronic noise in the cell. Therefore a random number X with a Gaussian distribution $G(X)$ is added to the measured energy in the following way:

$$E' = E + X \tag{7.2}$$

$$G(X) = \frac{1}{\sigma_E\sqrt{2\pi}} e^{-\frac{X^2}{2\sigma_E^2}} \tag{7.3}$$

This smearing has to be applied for every calorimeter cell involved in the energy measurement. Since this treatment was impossible in this analysis for technical reasons, an alternative method of noise treatment was developed. In this method, the correction factor X in equation 7.2 is calculated once per probe muon candidate for the largest cone size value of $\Delta R_{max} = 0.45$ by adding up the correction factors for each calorimeter layer (see section 6.3) in quadrature. The correction factor for the smaller cone sizes ΔR_i is then calculated by scaling X down according to the smaller transverse section of the cone, taking the pseudorapidity η of the probe muon candidate into account:

$$\begin{aligned} X' &= X \cdot C \\ &= X \cdot \frac{\tan \Delta R_i \cdot \frac{2e^{\Delta R_i} - a(1+2e^{\Delta R_i})+1}{e^{-\eta}-e^{\Delta R_i+\eta}}}{\tan \Delta R_{max} \cdot \frac{2e^{\Delta R_{max}} - b(1+2e^{\Delta R_{max}})+1}{e^{-\eta}-e^{\Delta R_{max}+\eta}}} \\ a &= \frac{e^{2\Delta R_i} + 2e^{\Delta R_i} + 1}{e^{-2\eta} - 2e^{\Delta R_i} + e^{\Delta R_i^2+\eta^2+2\Delta R_i\eta}} \\ b &= \frac{e^{2\Delta R_{max}} + 2e^{\Delta R_{max}} + 1}{e^{-2\eta} - 2e^{\Delta R_{max}} + e^{\Delta R_{max}^2+\eta^2+2\Delta R_{max}\eta}} \end{aligned} \tag{7.4}$$

The smeared energy was then used as an input for the calorimeter isolation criterion and the $E_T/p_{t,\mu}$ isolation criterion.

The track reconstruction efficiency as systematic uncertainty for the track isolation criterion was treated in a similar way. The measured number of tracks was folded with a Gaussian distribution analogous to equation 7.2. The width of the Gaussian was set to the track reconstruction uncertainty of 1%, multiplied with the number of reconstructed tracks.

The resulting systematic deviations for the calorimeter isolation criterion and the $E_T/p_{t,\mu}$ isolation criterion at a fixed cut value is presented in table 7.2.

The track reconstruction uncertainty showed no impact on the track isolation efficiency. The overall shape of the isolation efficiency distributions for all three criteria is not affected

calorimeter isolation criterion				
cut value	cone size	ϵ w/o systematics	ϵ with systematics	deviation
$1GeV$	0.1	0.8212	0.8181	0.0031
	0.15	0.7577	0.7504	0.0073
	0.2	0.6455	0.6280	0.0175
	0.25	0.6089	0.5713	0.0376
	0.3	0.5667	0.5029	0.0638
	0.35	0.5178	0.4323	0.0855
	0.4	0.4646	0.3600	0.1046
	0.45	0.4190	0.3006	0.1184
$E_T/p_{t,\mu}$ isolation criterion				
cut value	cone size	ϵ w/o systematics	ϵ with systematics	deviation
0.06	0.1	0.9356	0.9251	0.0105
	0.15	0.8253	0.8111	0.0142
	0.2	0.8081	0.7873	0.0212
	0.25	0.7883	0.7604	0.0279
	0.3	0.7654	0.7308	0.0348
	0.35	0.7365	0.6933	0.0432
	0.4	0.7023	0.6459	0.0564
	0.45	0.6658	0.5996	0.0662

Table 7.2: Changes in the isolation efficiencies if systematic effects are taken into account.

by the considered systematic effects.

The $E_T/p_{t,\mu}$ isolation criterion proves to be more stable than the pure calorimeter isolation criterion under the systematic effect of the energy measurement uncertainty caused by electronic calorimeter noise. The step in isolation efficiency for the $E_T/p_{t,\mu}$ criterion between cone sizes of 0.1 and 0.15 is an effect of the single QCD background event.

The deviations for both the calorimeter isolation criterion and the $E_T/p_{t,\mu}$ isolation criterion increase with rising cone size, as more calorimeter cells are then used in the calculation of the electronic noise. On the other side the systematic effect of the calorimeter cell noise has less influence for larger cut values (i.e. higher energies around the muon candidate), since the noise is then a smaller percental fraction of the total energy. The $E_T/p_{t,\mu}$ criterion is less affected by the calorimeter cell noise than the pure calorimeter isolation criterion.

The corresponding graphs are shown in figure 7.4 for the calorimeter isolation criterion, figure 7.5 for the $E_T/p_{t,\mu}$ isolation criterion and figure 7.6 for the track siolation criterion.

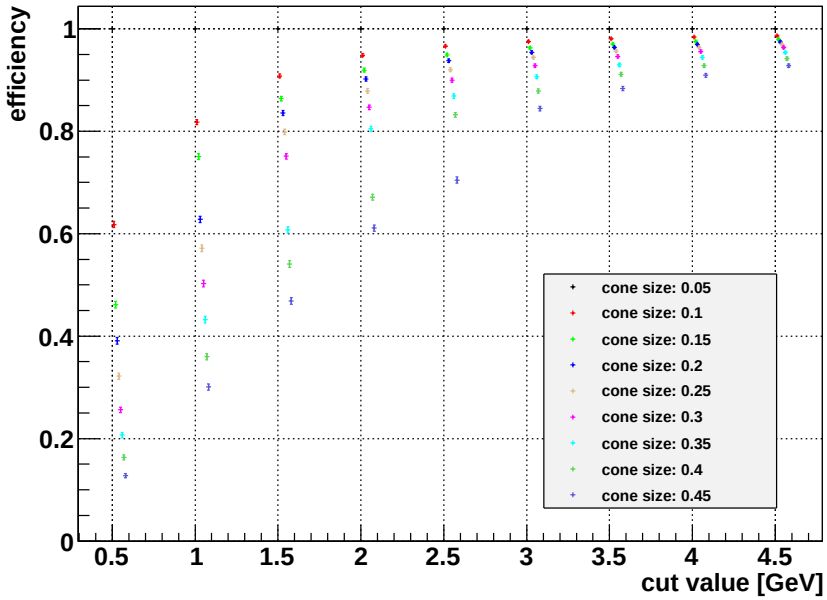

Figure 7.4: The impact of the Gaussian systematics approach on the calorimeter isolation efficiencies. For an example of the numeric deviations, see table 7.2.

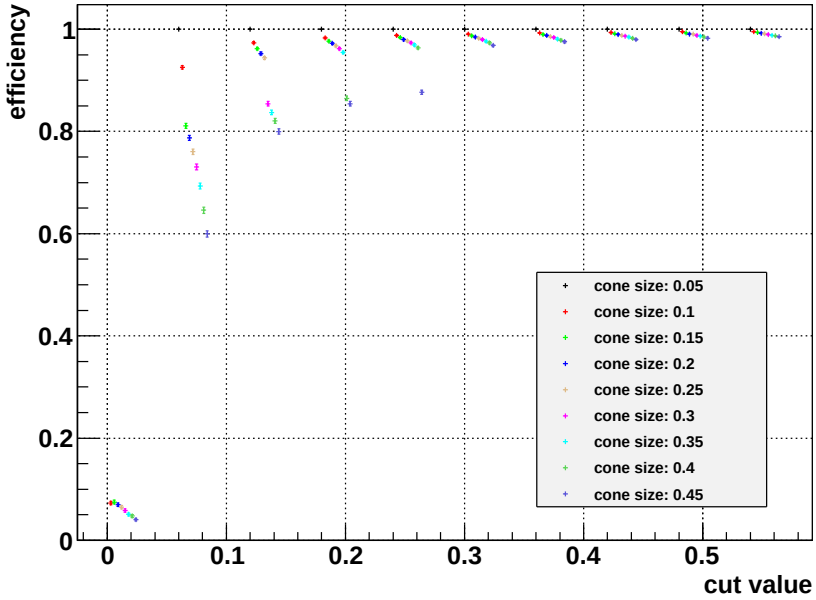

Figure 7.5: Gaussian energy systematics applied to the $E_T/p_{t,\mu}$ isolation criterion.

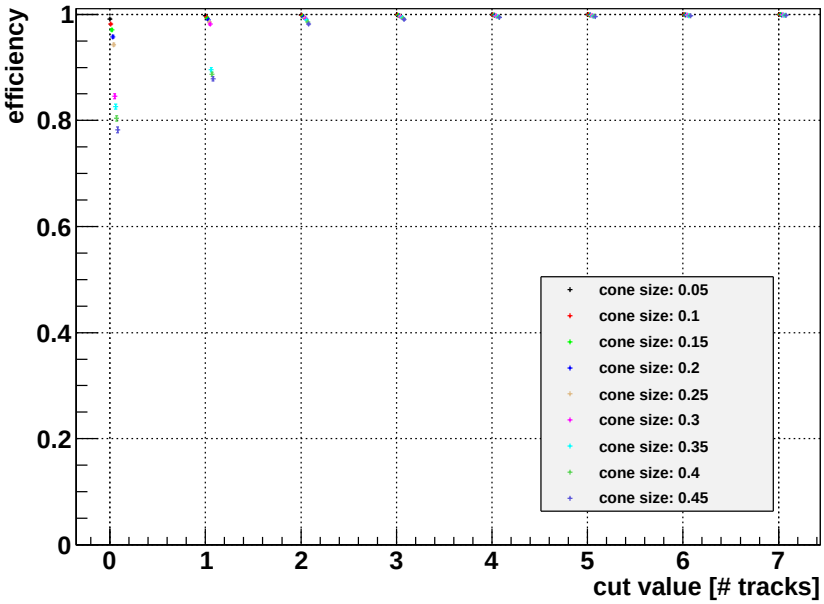

Figure 7.6: The influence of the systematics of the track reconstruction efficiency on the track isolation criterion. No effect is noticed

Chapter 8

Conclusion and Outlook

For the first time, a purely data-driven method to determine muon isolation efficiencies has been developed and investigated in ATLAS. Since muon isolation is an essential criterion for muons coming from heavy boson decays, the efficiency of an isolation criterion is of invaluable interest. This study begins with selecting a pure $Z^0 \rightarrow \mu\mu$ subsample from a mixture of data samples mimicking the expected composition of ATLAS collision data containing two reconstructed muon candidates. Subsequently, the muon isolation efficiency is determined by applying a "tag and probe" method on this subsample.

Isolation efficiencies have been obtained for three basic isolation criteria: the calorimeter isolation criterion, the track isolation criterion and the $E_T/p_{t,\mu}$ criterion. Their behavior under different settings of cone sizes and cut values was investigated, and the results are understood. It could be shown that even with a small integrated luminosity of $10pb^{-1}$, it will be possible to obtain enough statistics to reduce the statistical error to below 2%.

The track isolation criterion has proven to be most efficient and stable, the $E_T/p_{t,\mu}$ criterion has shown a good performance, the pure calorimeter isolation criterion seems weaker than the other two.

The investigation of systematic effects showed a moderate influence of the energy measurement uncertainty on the $E_T/p_{t,\mu}$ criterion, with a relative impact of $\approx 10\%$ maximum. This influence is larger for the pure calorimeter isolation criterion with a relative deviation of up to $\approx 29\%$. The track isolation criterion is not affected by the track reconstruction efficiency.

The influence of the sample impurity, though, could only be estimated. Further investigation on this impact are thus recommended. This issue could also be solved by tightening the sample selection cuts and thus improving the purity on the possible cost of statistic safety. Furthermore an isolation criterion has to be valued by its efficiency and its misidentification probability or fake rate, which should be subject to further studies.

The method presented in the thesis can be extended to include other isolation criteria, for example the CSC muon isolation criterion[13].

The isolation efficiency determination method developed in this thesis is a powerful tool for any isolation criterion. It could also be applied to other charged lepton reconstruction algorithms investigating data. Accompanied by a method to determine isolation fake rates, this is a vital instrument for any further analysis relying on the identification of isolated muons.

List of Figures

List of Tables

Bibliography

[1] D. Griffiths, "Introduction to elementary particles," Weinheim, USA: Wiley-VCH (2008) 454 p.

[2] R. K. Ellis, W. J. Stirling, and B. R. Webber, "QCD and collider physics," *Camb. Monogr. Part. Phys. Nucl. Phys. Cosmol.*, vol. 8, pp. 1–435, 1996.

[3] V. A. Bednyakov, N. D. Giokaris, and A. V. Bednyakov, "On Higgs mass generation mechanism in the standard model," *Phys. Part. Nucl.*, vol. 39, pp. 13–36, 2008.

[4] C. Amsler et al.(Particle Data Group) *Physics Letters B667*, vol. 1, 2008.

[5] J. Collins, D. Soper, and G. Sterman, "Factorization of Hard Process in QCD," *High Energy Phys. 5*, 1988.

[6] P. M. Nadolsky, "Theory of W and Z boson production," *AIP Conf. Proc.*, vol. 753, pp. 158–170, 2005.

[7] A. D. Martin, R. G. Roberts, W. J. Stirling, and R. S. Thorne, "Uncertainties of predictions from parton distributions. I: Theoretical errors," *Eur. Phys. J.*, vol. C35, pp. 325–348, 2004.

[8] A. M. de Goursac, "Noncommutative geometry, gauge theory and renormalization," 2009.

[9] F. Halzen and A. Martin, "Quarks and Leptons," *John Wiley & Sons*, 1984.

[10] A. D. Martin, W. J. Stirling, R. S. Thorne, and G. Watt, "Parton distributions for the LHC," *Eur. Phys. J.*, vol. C63, pp. 189–285, 2009.

[11] CERN, "LHC structure," *LHC-PHO-1997-203*, 1997.

[12] S. Meyers, "LHC Status," 2009.

[13] G. Aad *et al.*, "Expected Performance of the ATLAS Experiment - Detector, Trigger and Physics," 2009.

[14] CERN, "Computer generated image of the ATLAS inner detector," *CERN-GE-0803014*, 2008.

[15] CERN, "Computer Generated image of the ATLAS calorimeter," *CERN-GE-0803015*, 2008.

[16] CERN, "Computer generated image of the ATLAS Muons subsystem," *CERN-GE-0803017*, 2008.

[17] I. Dawson and K. Prokofiev, "Determining the inelastic proton-proton cross section at the Large Hadron Collider using minimum bias events," *Eur. Phys. J.*, vol. C51, pp. 1009–1012, 2007.

[18] G. Aad *et al.*, "The ATLAS Experiment at the CERN Large Hadron Collider," *JINST*, vol. 3, p. S08003, 2008.

[19] I. Consortium, "ATLAS TDAQ architecture," *http://dissemination.interactive-grid.eu/*, 2006.

[20] G. Duckeck, (ed.) *et al.*, "ATLAS computing: Technical design report," CERN-LHCC-2005-022.

[21] CERN, "Athena - The ATLAS Common Framework," vol. 3, 2002.

[22] U. Baur, B. A. Kniehl, J. A. M. Vermaseren, and D. Zeppenfeld, "Single W and Z production at LEP / LHC," Contribution to Proc. of Large Hadron Collider Workshop, Aachen, Germany, Oct 4-9, 1990.

[23] C. Anastasiou, L. J. Dixon, K. Melnikov, and F. Petriello, "High precision QCD at hadron colliders: Electroweak gauge boson rapidity distributions at NNLO," *Phys. Rev.*, vol. D69, p. 094008, 2004.

[24] M. L. Mangano, M. Moretti, F. Piccinini, R. Pittau, and A. D. Polosa, "ALPGEN, a generator for hard multiparton processes in hadronic collisions," *JHEP*, vol. 07, p. 001, 2003.

[25] M. Lamont, "LHC: status and commissioning plans," 2009.

[26] I. van Vulpen, "Binomial Error intervals and extra leptons in ttbar events," *NIKHEF PAT meeting*, 2007.

[27] K. A. Assamagan, "The muon ESD packages," *The LXR Cross Referencer.*

[28] K. A. Assamagan, "IsolationTools," *ATLAS TWiki.*

[29] C. A. et al., "CaloUtils Package," *The LXR Cross Referencer.*

Danksagung

An dieser Stelle möchte ich mich bei allen Personen bedanken, die zur Anfertigung der Diplomarbeit beigetragen haben. Zuerst möchte ich mich bei meinen Betreuern Prof. Dr. Michael Kobel und Dr. Wolfgang Mader bedanken, die mir die Arbeit am Institut für Kern- und Teilchenphysik und Bearbeitung eines Themas der aktuellen Forschung im Bereich der Teilchenphysik ermöglicht haben.

Mein Dank gilt weiterhin der gesamten Teilchenphysik-Gruppe des IKTP, die mir bei Problemen immer mit Ratschlägen zur Seite stand. Besonders hervorheben möchte ich hier das Engagement von Peter Steinbach, Thomas Göpfert und Dr. Anja Vest, die mich sowohl bei der Anfertigung der Arbeit selbst als auch in der Methodik und bei physikalischen Fragen unterstützten.

Auch meinen Freunden und insbesondere meinen Eltern und meiner Schwester danke ich für den Rückhalt, das Interesse an meiner Tätigkeit und die teilweise notwendigen Motivationsschübe.

Und ganz besonderen Dank richte ich an Diana Reinhardt, die immer für mich da war wenn ich sie brauchte und mich auch in schwierigen Zeiten unterstützte und motivierte.

Selbstständigkeitserklärung

Ich versichere hiermit, die vorliegende Arbeit selbstständig und ohne unzulässige Hilfe Dritter angefertigt zu haben. Es wurden keine anderen als die angegebenen Hilfsmittel und Quellen verwendet. Resultate, die aus fremden Quellen direkt oder indirekt übernommen wurden, sind als solche kenntlich gemacht worden.

Dresden, den 30.11.2009

Christian Rudolph